THE PENNSYLVANIA STATE UNIVERSITY
SCHREYER HONORS COLLEGE

DEPARTMENT OF ENGINEERING SCIENCE AND MECHANICS AND DEPARTMENT OF PHYSICS

AN INVESTIGATION OF ENHANCED RAMAN SCATTERING ON 2D MATERIAL SUBSTRATES

VIVEK ANIL
SPRING 2020

A thesis
submitted in partial fulfillment
of the requirements
for baccalaureate degrees
in Engineering Science and Physics
with interdisciplinary honors in Engineering Science and Physics

Reviewed and approved* by the following:

Mauricio Terrones
Verne M. Willaman Professor of Physics
Thesis Supervisor

Reginald Hamilton
Associate Professor of Engineering Science and Mechanics
Honors Adviser

Richard W. Robinett
Professor of Physics
Honors Adviser

Judith A. Todd
Department Chair
P. B. Breneman Chair and Professor of Engineering Science and Mechanics

* Electronic approvals are on file.

ABSTRACT

Non-technical:

Graphene has demonstrated the ability to enhance Raman signals from low concentrations of adsorbed molecules; this phenomenon is known as graphene enhanced Raman scattering (GERS). More recently, other 2D materials, such as MoS_2, have also demonstrated this Raman-enhancing ability. Compared to other similar platforms, such as surface enhanced Raman spectroscopy (SERS) which makes use of metallic nanoparticles, 2D materials are more biocompatible, and so the Raman-enhancing effect on 2D materials offers promise for biosensing applications. While this phenomenon has been demonstrated on 2D materials, questions remain about the mechanism of enhanced Raman scattering. This study seeks to provide experimental data that could be used to assess a proposed mechanism for enhanced Raman scattering on 2D materials based on a charge transfer between the 2D substrate and the adsorbed molecule. Further, this charge transfer mechanism is strengthened by aligning an energy level in the substrate with an energy level in the molecule and using a laser with energy approximately equal to the energy gap in the molecules. We synthesize 2D material substrates, graphene and WS_2, and prepare fluorescent dyes and collect Raman spectra of these dyes adsorbed on the substrates with different lasers. We compare the ability of each substrate to probe vibrational modes of each of the dyes. Our results give support for the proposed mechanism not only in graphene, but also in WS_2.

Technical:

Previous research asserts that the observation of enhanced Raman signals from molecules adsorbed on graphene and doped graphene substrates are due to charge transfer between

graphene and the molecules. It is further proposed that this charge transfer is strengthened by the alignment of the molecule's LUMO with graphene's Fermi energy and an excitation nearly resonant with the HOMO-LUMO gap of the molecule. More recently, other 2D materials have similarly shown the ability to enhance Raman signals from adsorbed analytes. This research seeks to test the aforementioned proposed charge transfer mechanism by collecting Raman spectra of fluorescent dye solutions, 10^{-5} M crystal violet (CV), 10^{-5} M rhodamine 6G (R6G), and 10^{-5} M rhodamine B (RhB), on graphene and WS_2 substrates at different laser excitations. Based on the charge transfer mechanism, we develop a hypothesis for which combinations of dyes, substrates, and lasers would allow us to observe the best Raman enhancement of the dyes' vibrational modes. For CV, we observed a few vibrational modes on graphene and none on WS_2, for R6G many modes on WS_2 and some on graphene, and for RhB some modes on WS_2 but fewer on graphene. In addition, the ability of the substrates to quench the fluorescence of the dyes was influenced by energy-level alignment. Our results were mostly in agreement with our hypothesis and therefore give support to the proposed mechanism in graphene as well as its extension to WS_2.

TABLE OF CONTENTS

LIST OF FIGURES

LIST OF TABLES

ACKNOWLEDGEMENTS

I would like to thank Professor Terrones for supervising my thesis, for giving me the opportunity to work in his lab and on this project, and for taking the time to meet with me and discuss this research. I would also like to thank all the postdoctoral fellows and graduate students in our group who took the time to mentor me in the lab. In particular, I would like to thank He (Moses) Liu, Tomotaroh Granzier-Nakajima, Mingzu Liu, Edgar Dimitrov, and Professor Yin-Ting (Tim) Yeh. Moses spent the most time helping me on this project: taught me how the prepare the fluorescent dye solutions, helped me carry out Raman experiments on the Horiba LabRam Evolution Spectrometer, and took the time to meet with me and discuss ideas and the direction of the research. Tomotaroh Granzier-Nakajima provided me with graphene samples, taught me his method for graphene transfers, and helped me understand the Raman spectra I collected on graphene samples. Mingzu provided me with WS_2 samples and met with me to discuss the synthesis. Edgar was almost always present in the lab when I was working, and he was very helpful in problem-solving challenges with my graphene transfer and finding instruments in the lab. Though I did not work with Tim much on this project, the time I spent working with and learning from him on previous projects during my first experiences with research were instrumental in sparking my desire to continue research and go to graduate school; I am very grateful for his mentorship. Finally, I would like to thank my honors advisers, Professor Robinett and Professor Hamilton, as well as my other professors and instructors in the Engineering Science and Mechanics and Physics departments for four wonderful years.

Chapter 1

Introduction

Problem Statement

Raman spectroscopy provides an approach to molecular identification that is noninvasive, fast, and easy to reproduce. However, the signal intensity from Raman spectra is often weak, making it difficult to detect low concentrations of the analyte. To address the need for signal enhancement, researchers have used Au and Ag nanoparticles to enhance spectra in a technique called surface-enhanced Raman spectroscopy (SERS). However, the plasmonic metals used as enhancing substrates in SERS are easily oxidized and not biocompatible [1]. 2D materials would be ideal Raman enhancing substrates as they are flat (no dangling bonds so there is no direct chemical bonding with the analyte), mostly biocompatible, flexible, and easy to integrate into technologies [2]. Furthermore, previous studies have shown promise for amplifying Raman signals with 2D materials [1,2]. Still, the mechanism of Raman enhancement provided by 2D materials is not entirely understood; this study aims to further understanding of this enhancement mechanism.

Design Needs

The tools employed in this study include walk-in hoods and furnaces with temperature controls for atmospheric pressure chemical vapor deposition synthesis of graphene and WS_2, lasers and Raman spectrometers, and MATLAB for subtracting noise and plotting spectral data.

Executing these experiments involved numerous design choices. For instance, modifications to flow rates of precursor gases and annealing and growth temperatures and times were made for the optimal synthesis of 2D materials. Graphene was chosen as one of 2D material substrates as prior experimental literature could serve as a reference for this study as well as the extension of this study to a less explored Raman enhancing substrate, WS_2. We chose to use fluorescent dyes in these experiments to explore the ability of 2D materials to suppress fluorescent background. For the purpose of testing our hypothesis, specific fluorescent dyes were chosen for the position of their energy levels relative to the Fermi energies of the 2D material substrates. Then, the lasers employed in the Raman experiments were chosen to correspond to the gaps between energy levels in the dyes. The processes of preparing and adsorbing the dyes were designed to optimize our ability to probe the characteristic vibrational modes in each dye.

The science explored in this research has potential for broader positive impacts on society and public health. The understanding of the Raman enhancing mechanism in 2D material substrates would allow us to better engineer 2D materials as sensors for biological molecules, and thereby lead to the development of devices for disease diagnosis. This Raman spectroscopy-based approach would provide a rapid, non-invasive platform for diagnosis. Protocols set by Penn State Environmental Health and Safety were adhered to in conducting this experimental study to ensure safe laboratory and environmental practices. In keeping with professional ethics, care has been taken to cite and acknowledge previous research referenced in this thesis. This research did not specifically study questions of ethical responsibility or economic issues, and hence these are not specifically addressed in this thesis.

Thesis Objectives

In this work, the Raman enhancement capabilities of different 2D material substrates are investigated. The 2D materials studied are graphene and WS_2. The spectra of fluorescent dye solutions, 10^{-5} M crystal violet, 10^{-5} M rhodamine 6G, and 10^{-5} M rhodamine B, are obtained on these substrates by adsorbing the dyes onto the 2D materials. Furthermore, different laser excitations are experimented with in an attempt to best enhance the Raman signal and elucidate the mechanism of Raman enhancement for each system. The results are useful for improved understanding of enhanced Raman spectroscopy as well as furthering its potential for use in biosensing applications.

Chapter 2

Literature Review

Overview of 2D Materials: Properties, Synthesis, and Applications

2D materials exhibit an array of properties that are not seen in their bulk counterparts. Since the discovery of the first 2D material, graphene, in 2004 [3], these single layer crystalline structures have been widely researched for their potential in diverse applications, including semiconductor electronics [4], photovoltaics [5], electrodes [6], optoelectronics [7], nanoelectromechanical systems [8], and molecular sensing [1,8–10]. Table 1 provides an overview of electronic properties and synthesis methods for 2D materials.

Table 1: Overview of electronic properties and synthesis of 2D materials; images from graphene and h-BN are from [2] and the image for TMDs is from [11].

2D material	**Graphene** 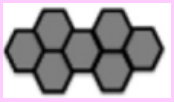	**Hexagonal boron nitride (h-BN)** 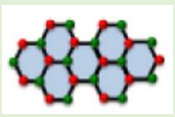	**Transition metal dichalcogenides (MX_2)** 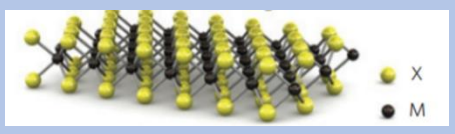
Electronic Characteristics	• Zero bandgap semi-metal with near zero effective mass near Dirac points [12] • Can dope to open up bandgap [9,13–15] • n type dopant: N, p type dopant: B [15]	• Insulator • Bulk bandgap 6.08 eV and indirect [16] • Monolayer bandgap ~6.5 eV and crosses over to direct [16]	• NbS_2, $NbSe_2$, $NbTe_2$, TaS_2, $TaSe_2$, and $TaTe_2$ are metallic or can exhibit exotic superconducting or charge density wave properties [11] • WS_2, WSe_2, WTe_2, MoS_2, $MoSe_2$, and$MoTe_2$ are semiconducting and their bandgaps are dependent on the number of layers; bulk bandgaps are indirect, but monolayer bandgaps become direct [11]

			• Monolayer bandgaps: WS_2 (1.9 eV), WSe_2 (1.7 eV), MoS_2 (1.8 eV), $MoSe_2$ (1.5 eV) [11]
Common Synthesis Methods	• Exfoliation [3], chemical vapor deposition [17, 18]	• Chemical vapor deposition [19], pulsed laser deposition, reactive magnetron sputtering, and molecular beam epitaxy [20]	• Mechanical exfoliation, chemical vapor deposition [11,21]

Graphene

Graphene, a two-dimensional allotrope of carbon with atoms arranged in a hexagonal lattice, is heralded for its electronic, optical, thermal, and mechanical properties [12,17,22]. For instance, graphene sheets have demonstrated an unusually high opacity (absorption ratio of ~2.3% white light) and resistivities less than that of silver, the metal with the lowest known room temperature resistivity [17].

The unique properties of graphene are due largely to its sp^2-hybridization, which leaves the fourth valence electron in carbon in an unhybridized p_z orbital and allows for the formation of π-bonds, as shown in Figure 1 [17]. These π-bonds hybridize in turn to form a filled π (valence) and unfilled π*(conduction) bands. The distinct band structure in graphene contributes to its novel electronic and optical properties [12,17].

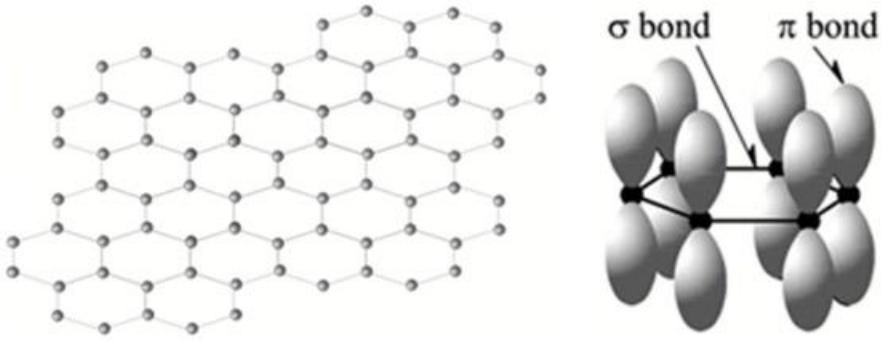

Figure 1: (Left) Graphene's hexagonal lattice; (Right) In-plane σ-bonds and out-of-plane π-orbitals in graphene [17].

In pristine graphene, the conduction and valence bands intersect at K and K' points in the Brillouin zone (see Figure 2). These intersecting points are also known as Dirac points and the conduction and valence bands are linear in this region, forming Dirac cones. Because the bands in graphene intersect with the Fermi level at the Dirac point, graphene is a zero-band gap semimetal [12]. In addition to the zero-band gap, the linear shape of the bands also means electrons in graphene exhibit near zero effective mass (charge carriers can be described as massless Dirac fermions), which explains its extraordinary electron mobility [12,17]. In their groundbreaking experiments on graphene's electrical properties, Nobel Prize-winners, Novoselov and Geim, reported room temperature mobilities of ~10000 $cm^2 V^{-1}s^{-1}$ [3].

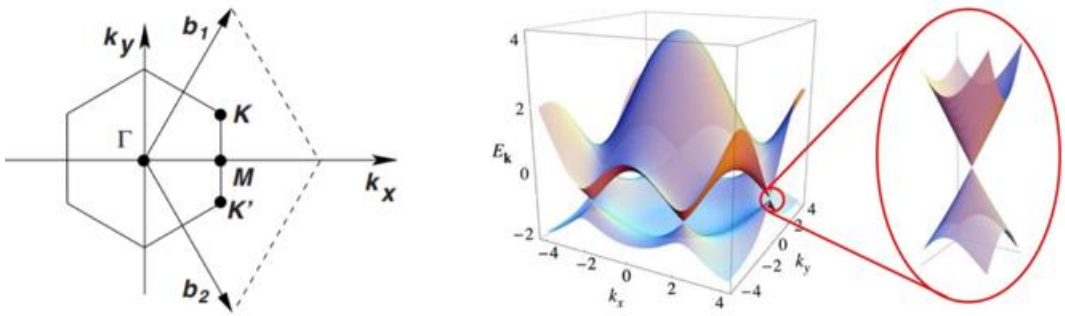

Figure 2: (Left) Graphene's Brillouin zone; (Right) E-k dispersion of graphene's honeycomb lattice with meeting of Dirac cones magnified [12].

Though it was observed as an adsorbate on metallic surfaces via electron microscopy in 1962 [23], graphene was first isolated by Novoselov and Geim in 2004 [3]. Novoselov and Geim used mechanical exfoliation with “scotch tape” to perform this isolation [3]. Mechanical exfoliation is a top-down approach that uses mechanical force to break the van der Waals bonds in graphite and separate out the individual graphene sheets. This method makes it possible to obtain one to a few layers of graphene. However, it is not suitable for large scale production of graphene and is not reliable in producing the same quality graphene consistently [17,18,24].

In contrast to exfoliation, chemical vapor deposition (CVD) is a bottom-up approach which involves the flow of precursor gases into a tube furnace. These gases react at high temperatures to initiate the deposition of a product on a substrate [17]. CVD graphene is normally grown using a methane gas precursor and copper or nickel foil substrates. The advantages of CVD are that it produces a large surface area, high quality graphene with good electrical conductivity and optical transparency. These characteristics make CVD the most favorable method of synthesizing graphene for most applications. The disadvantages of CVD are that it occurs at high temperature and is sensitive to unstable gas flow and small changes in temperature. As a result of these fragile growth parameters, positioning of the substrate in the growth chamber is an important factor in the quality of CVD graphene. CVD also involves an additional process to transfer the graphene from the growth substrate to silicon or glass for use in many device applications [18].

The novel electronic properties of graphene have led to it being widely researched for potential applications. However, the zero-band gap also has drawbacks when it comes to using graphene in electronic and optoelectronic devices. For instance, without a bandgap, graphene

cannot have an “on” and “off” state (where “on” corresponds to the application of a threshold voltage that exceeds the bandgap energy; graphene remains “on” all the time), and so it is difficult to make a transistor-like device that utilizes graphene [14]. Though pristine graphene exhibits many wonderful properties, these drawbacks have spurred researchers to investigate variants of graphene and other 2D materials that complement the properties of pristine graphene.

Doped Graphene

Heteroatom doping in silicon has been used to modulate its electronic properties for semiconductor applications. Likewise, doping graphene with nitrogen, boron, phosphorous, sulfur, chlorine, fluorine, bromine, silicon, and germanium has also been investigated to modulate its electronic, chemical, catalytic, and optical properties [9,13–15]. Since graphene is a 2D material, there is no variation of dopant concentration with depth. CVD is a common method for in situ doping of graphene. Post growth doping methods include ion implantation and plasma treatments [15].

Nitrogen and boron are the dopants most commonly incorporated into graphene because boron and nitrogen are next to carbon in the periodic table. This indicates that boron and nitrogen have similar atomic radii to C atoms and form bonds with C atoms that are similar length to the C-C bonds in graphene. Thus, boron and nitrogen can easily substitute for carbon in the graphene lattice. Nitrogen doped graphene (NG) opens up a band gap and raises the Fermi level into the conduction band, and thereby exhibits n-type behavior. Conversely, boron doped graphene (BG)

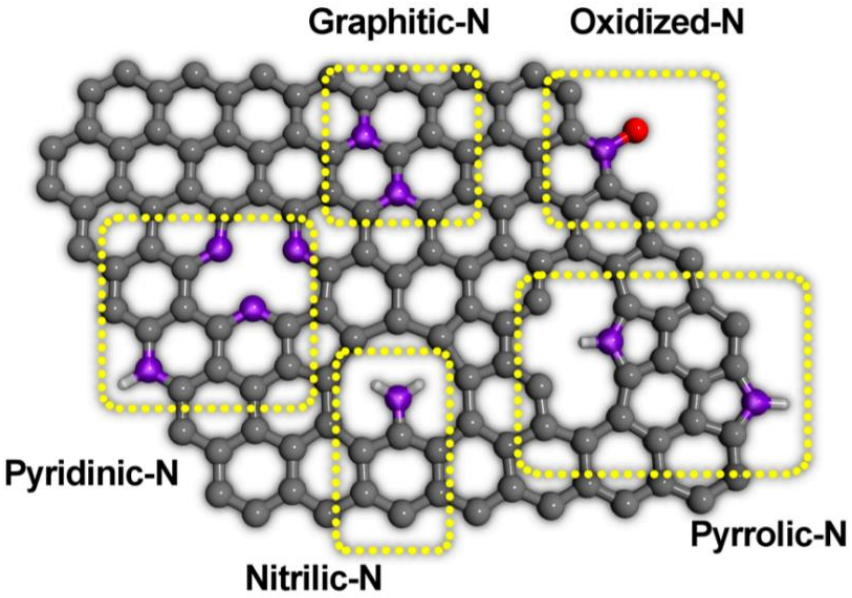

Figure 3: Different doping configurations of nitrogen in graphene [15].

induces p-type conductivity [15,25]. Though less explored than NG and BG, other forms of doped graphene, such as silicon doped graphene, can also open up a bandgap [26].

Heteroatoms can be added into the graphene lattice in different configurations, depending on the preparation method. In NG, these configurations include graphitic-N, pyridinic-N, pyrrolic-N, nitrilic-N, and oxidized-N, all shown in Figure 3 [15].

Different dopant configurations alter the local charge distribution and density of states and thereby produce different electronic, catalytic, and sensing properties [15].

Atomically Thin Hexagonal Boron Nitride

Atomically thin hexagonal boron nitride (h-BN) is another graphene-like material that has drawn interest. Though structurally very similar to graphene, it is insulating and has proven

to be an excellent dielectric substrate for surface enhanced Raman spectroscopy and electronic devices made from 2D heterostructures. h-BN is also well regarded for its mechanical strength, thermal properties, and better surface adsorption than its bulk counterpart. Its strong high temperature oxidation resistance has demonstrated the ability to protect metals from oxidation and corrosion [27].

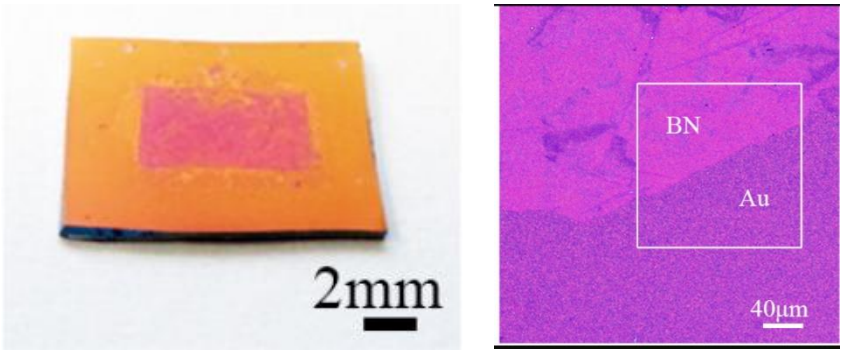

Figure 4: (Left) Photo of h-BN nanosheet grown on Au; (Right) Optical microscopy image of h-BN nanosheet on Au [19].

CVD is the most commonly used method to grow h-BN nanosheets; it has been carried out on catalytic mono or polycrystalline transition metal substrates, such as Cu, Ni, and Pt. The synthesis of thicker h-BN films on dielectric substrates, such as Al_2O_3, using metal organic CVD has also been demonstrated (see CVD grown h-BN in Figure 4 [19]). Other methods of synthesizing h-BN include pulsed laser deposition, reactive magnetron sputtering, and molecular beam epitaxy [20].

Monolayer Transition Metal Dichalcogenides

Unlike graphene, monolayers of transition metal dichalcogenides (monolayer TMDs), a family of 2D materials, have direct band gaps and lack inversion symmetry—giving these

materials fascinating electronic and optical properties. Many 2D TMDs have band gaps around 1-2 eV, which has made them attractive for developing novel field effect transistors, photodetectors, and electroluminescent devices [6,11].

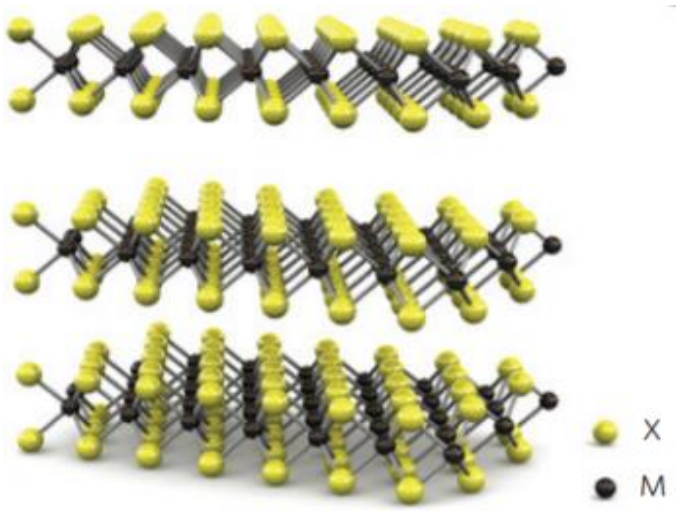

Figure 5: Ball-and-stick model of TMD layers [11].

Monolayer TMDs consist of a transition metal, M (such as Mo or W), covalently bonded to a chalcogenide X (S, Se, or Te), with the formula MX_2. Layered structures of these materials are of the form X-M-X; chalcogen atoms reside in hexagonal planes above and below a plane of the metallic atoms as shown in Figure 5. Individual layers are held together by van der Waals interactions, just like graphene and other 2D materials [11].

The most common methods for obtaining monolayer TMDs are top-down mechanical exfoliation and bottom-up CVD. Mechanical exfoliation is accomplished using a technique similar to the "scotch tape" method mentioned above for graphene. CVD offers much more promise for higher purity, larger area monolayer TMDs, and therefore holds more promise for synthesizing TMDs for electronic applications. The most frequently studied monolayer TMD, MoS_2, is often grown by CVD using a MoO_3 solid powder precursor [11,21].

Raman Spectroscopy

Raman Spectroscopy is a powerful and non-destructive technique used to identify and characterize materials [28,29]. It has demonstrated the capability to characterize material structure and properties including band structures, strain effects, doping type, electron–phonon coupling, and interlayer coupling [29]. The technique is based on a light scattering effect that was discovered by Indian physicist, Sir Chandrashekhara Venkata Raman, and his student, Sir Kariamanickam Srinivasa Krishnan, in 1928. Raman was awarded the 1930 Nobel Prize in Physics for this discovery. Today, extensive Raman libraries allow researchers to "fingerprint" a molecule by matching it to its Raman spectrum [28].

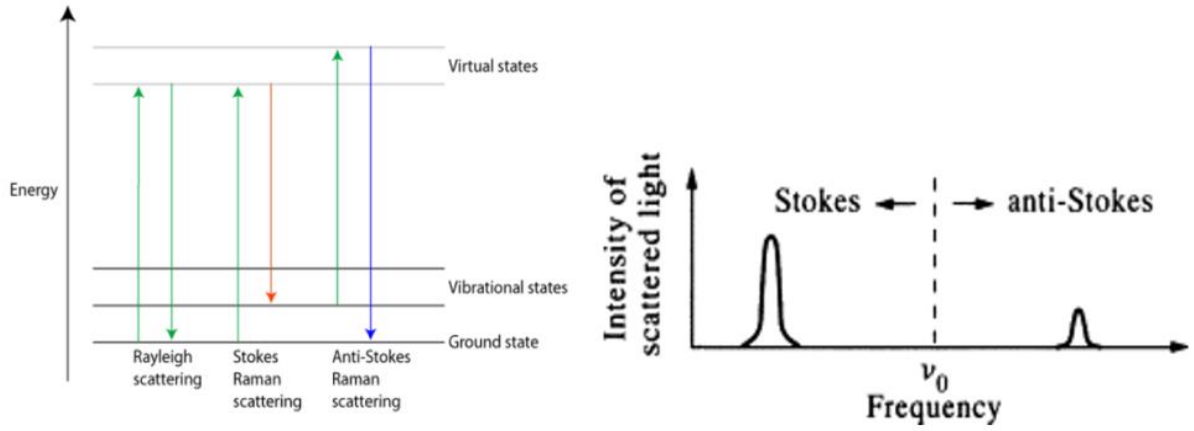

Figure 6: Generalized energy level diagram of Rayleigh, Stokes, and anti-Stokes Raman scattering (left) [30]; generalized intensity versus wavelength plot for Stokes and anti-Stokes Raman scattering (right) [31].

Normally, when light interacts with a material, there is no net transfer of energy between the light and the material, and so the scattered light leaves the material with the same energy as the incident light; this sort of scattering, known as Rayleigh scattering, is an elastic process that occurs for almost all incident photons. About one in every one million photons, however, undergo Raman scattering [28]. Raman scattering is an inelastic process that occurs when

incident photons interact with vibrational, or phonon, modes, resulting in a net energy transfer between the photon and the material. When an incident photon transfers energy to a material, leaving it in an excited vibrational energy state, the resulting scattered photon is of lower energy than the incident one; this is known as Stokes Raman scattering. In anti-Stokes Raman scattering, the material starts in an elevated vibrational energy state and gives up energy to the incident photon, leaving the material in a relaxed lower energy vibrational state. Thus, anti-Stokes Raman scattering results in the scattered photon being of higher energy than the incident one. According to the Boltzmann distribution, the majority of molecules exist in a lower energy state at room temperature, and so Stokes Raman scattering is more common than anti-Stokes Raman scattering. In general, the intensity of Raman scattering is much weaker than that of Rayleigh scattering as the latter is a much more common process for a light-material interaction [28,30,31]. The basic details of Raman and Rayleigh scattering are summarized in Figure 6.

Generally, in practice, Raman spectroscopy measures the intensity of scattered light versus the magnitude of the shift in wavenumber between the incident and scattered photons. The energy of the shift corresponds to the energy of the vibrational mode being probed in the material. Unlike most light-matter interactions, Raman excitations cause transitions between vibrational states and excited "virtual states," which unlike conventional quantum states, can exist at energies in between the discrete energy levels of a molecule. These virtual states are short lived (on the order of 10^{-13} seconds). Their existence can be explained by the presence of a strong electromagnetic field from the laser, and the fact that transitions between vibrational and virtual states rarely occur due to the low probability of Raman scattering. The significance of virtual states in Raman transitions is that in most cases, any Raman excitation will identify the

same vibrational modes, though with varying degrees of intensity depending on the laser energy [28].

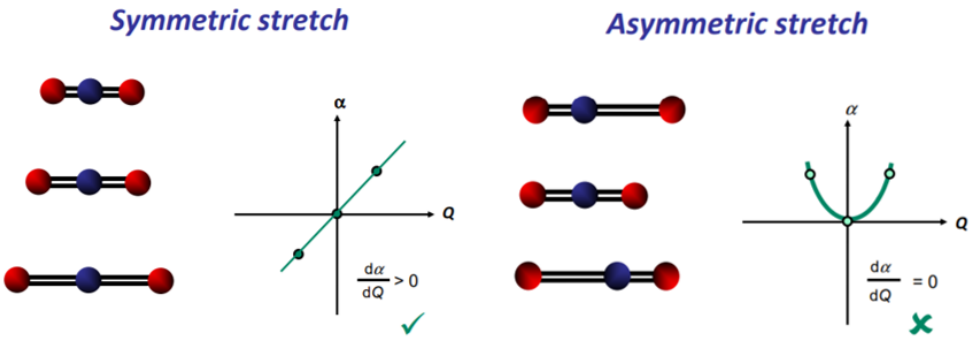

Figure 7: Symmetric molecular vibration (atoms being pulled apart and pushed together equal amounts) causing asymmetric change in polarizability; asymmetric stretches cause symmetric changes in polarizability [32].

The primary selection rule for Raman transitions asserts that for a particular vibrational mode to be "Raman active," the molecular polarizability must change asymmetrically during the molecular vibration (i.e. it must shift from large to small or from small to large). Polarizability is a term that describes the magnitude in the distortion of a molecule's electron cloud in the presence of an external electric field (see Figure 7 for asymmetric change in polarizability for a molecular vibration) [28,32].

Most vibrational modes tend to be either more Raman active than IR active (corresponding to the selection rules for infrared spectroscopic transitions) or vice versa. For centrosymmetric molecules, those that are symmetric about a central atom or point (see Figure 8 for more details on centrosymmetric molecules [33]), a given vibrational mode cannot be both Raman active and IR active. In general, symmetric vibrations tend to produce strong Raman signals and weak IR signals while asymmetric vibrations and bending vibrations produce the opposite [28,34].

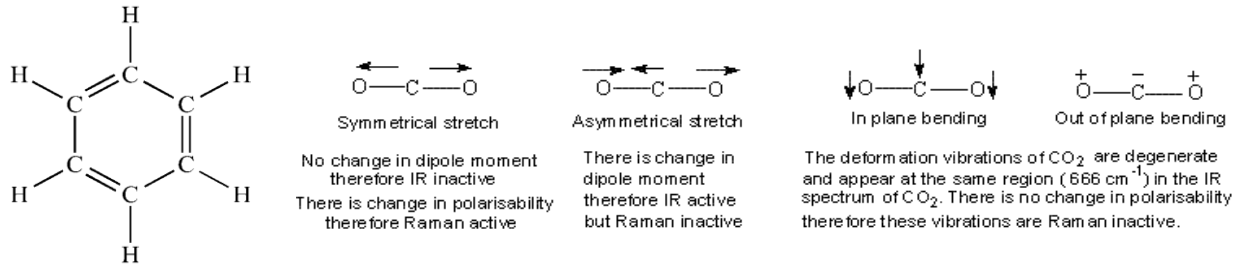

Figure 8: (Left) Benzene, a centrosymmetric molecule [33]; (Right) different vibrational modes of carbon dioxide, another centrosymmetric molecule--those modes that are IR inactive are Raman active, and vice versa [34].

To help predict the positions of vibrational modes in Raman, an atomic bond between two atoms can be modeled as two masses connected by a spring. Analyzing this simple configuration shows that the wavenumber corresponding to the oscillation is proportional to the square root of the spring constant divided by the reduced mass of the two atoms, where the spring constant corresponds to the bond strength between the two atoms. Thus, it can be inferred that stronger bonds and lighter atoms produce higher frequency vibrational modes. Hence, each molecule, being made up of different constituent atoms, bonding, and geometry, produce unique Raman spectra [28].

When obtaining Raman spectra of fluorescent molecules, it is best to avoid choosing excitation lasers that correspond to the transitions between energy levels in the molecule because the fluorescent background can interfere with and cloak the Raman signal [28]. However, for non-fluorescent molecules, tuning excitation lasers to match the electronic transitions in a molecule can significantly enhance Raman signals; this is known as resonance Raman spectroscopy [35].

Raman Spectra of 2D Materials

Features of Raman spectra can be used to identify and assess the crystalline quality of 2D materials. This section will briefly overview the characteristic Raman spectra from undoped and doped graphene, h-BN, and monolayer TMDs.

Graphene and Doped Graphene

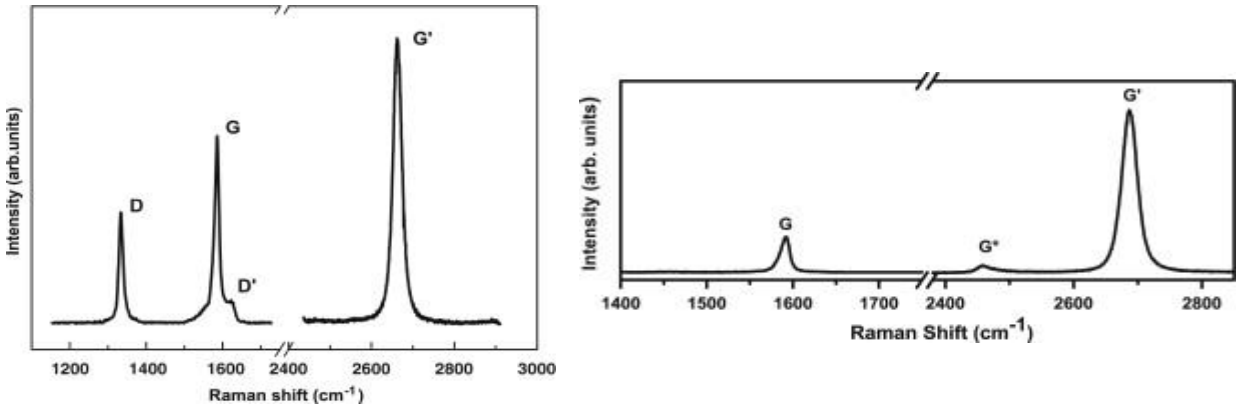

Figure 9: (Left) General Raman spectra of graphene; (Right) Raman spectra of pristine graphene (no D peak) [36].

The main features of graphene's Raman spectrum are a G-band at ~1582 cm^{-1}, a G'-band (also known as a 2D-band) at ~2700 cm^{-1}, and a D-band at ~1350 cm^{-1} [36,37] (see Figure 9). The G-band is attributed to the double-degeneracy of an in-plane transverse optical phonon mode and a longitudinal optical phonon mode at the Brillouin zone center; this is the only one of the three bands mentioned above that correspond to a first order Raman scattering process [36]. The D- and G'-bands are dispersive (dependent on laser excitation energy) and due to second order double resonance Raman processes. The D-band is due to an elastic scattering event between the incident photon and defects in the crystal and an inelastic scattering event that corresponds to emitting or absorbing a phonon. The G'-band is due to two inelastic scattering events, with each

event involving a phonon. The G'-band can also be understood from a triple resonance process, and in fact, this process serves well in explaining the large relative intensity of the G'-band compared to that of the G-band in monolayer graphene [36].

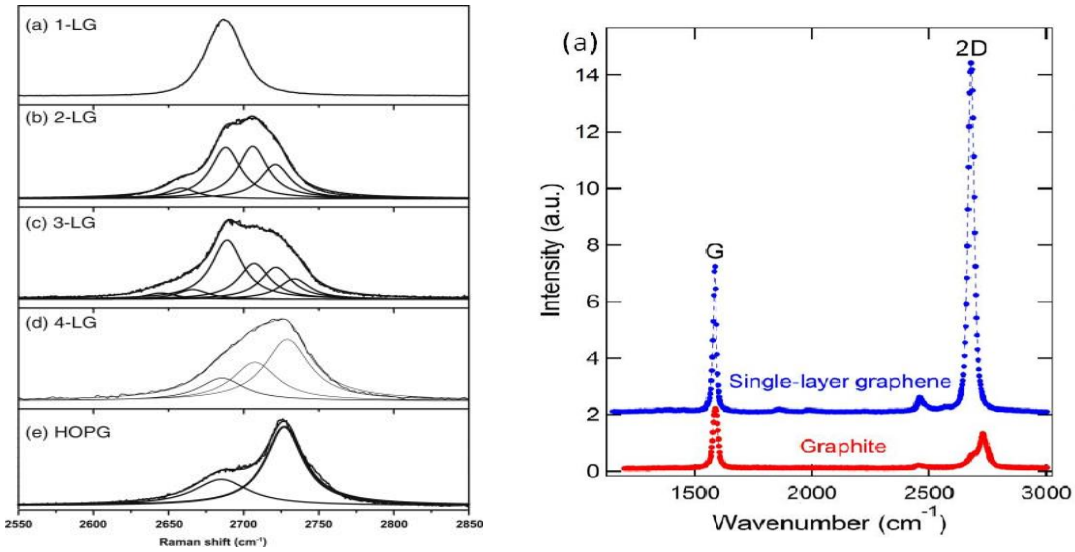

Figure 10: (Left) Splitting of G'-band [29]; (Right) Raman spectra of single layer pristine graphene and graphite--the ratio of the intensity for the 2D (G') to G peak is much higher for single layer graphene [37].

In A-B stacked graphene, as the number of graphene layers increase, the spectrum changes in that the G' peak splits into an increasing number of modes that interfere to produce a wider, shorter, higher frequency peak (see Figure 10); this splitting is correlated to the increased number of resonant processes for an increased number of layers of graphene [36,37]. Increased number of layers also causes the G peak to shift to slightly lower wavenumbers [37]. The ratio of the intensities of the G' and G peaks as well as the position and shapes of these peaks can be used to determine the number of layers of A-B stacked graphene. Unlike A-B stacked graphene, multilayer graphene with decoupled layers can have intense G' peaks compared to G peaks, but will deviate from monolayer graphene in the position and full width half maximum of these peaks [37].

By comparing the ratio of the intensities of the D peak to that of the G peak, one can characterize the level of disorder in graphene [37]. In high quality pristine graphene, the D peak will not be present. Increased disorder in graphene results in two different changes in the Raman spectrum. At low defect densities, the addition of more defects will cause more elastic scattering and thereby increase the intensity ratio of the D to G peaks. However, at high defect densities, there is a point where adding more defects causes an amorphous carbon structure, resulting in attenuation of all Raman peaks and a decrease in the intensity ratio of D to G peaks. Doping operates in the low defect density regime, and so increased D to G peak intensity ratios usually indicates that more dopants (defects) have been added to graphene [37]; this is corroborated by Figure 11, which shows the Raman spectra of NG with different dopant concentrations [15].

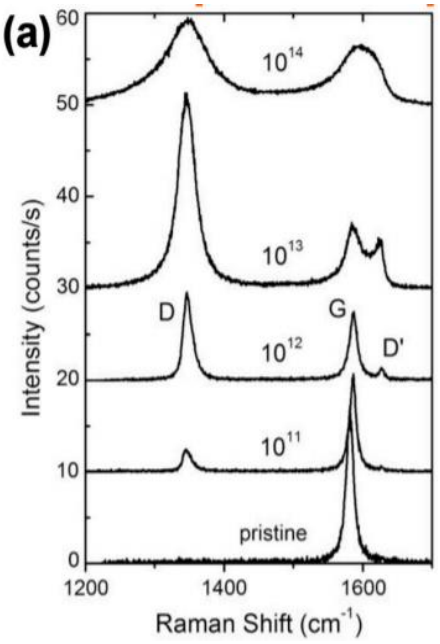

Figure 11: Raman spectra for different concentrations of nitrogen doping in graphene [15].

Hexagonal Boron Nitride

Unlike graphene, studies thus far have shown just one characteristic band for the Raman spectra of h-BN—the G-band at ~1370 cm^{-1}. Studies have shown that an increased number of layers of h-BN causes an increased intensity from this band, but very little shift in peak position (see Figure 12). However, strain does seem to cause a shift in peak position [38].

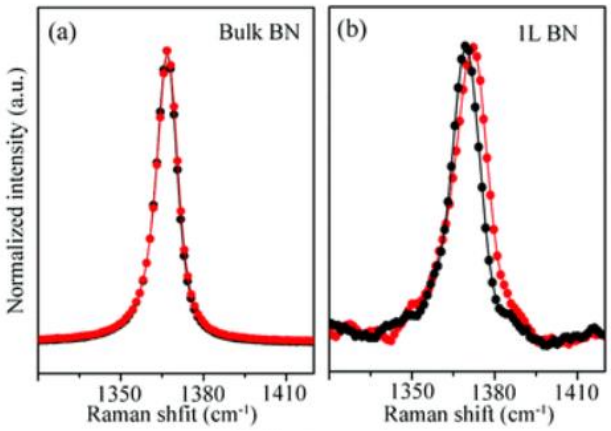

Figure 12: Raman spectra of h-BN for bulk and monolayer [38].

Monolayer Transition Metal Dichalcogenides

The number of layers in MoS_2, WS_2, WSe_2, and $MoSe_2$ are best correlated with the shifts in the E_{2g} and A_{1g} modes in the Raman spectra of these monolayer TMDs. The E_{2g} is at ~380 cm^{-1} and the A_{1g} mode is at ~410 cm^{-1} for MoS_2 [39,40]. Figure 13 summarizes the results of studies that investigated how the positions of these peaks varied with increased number of layers in TMDs.

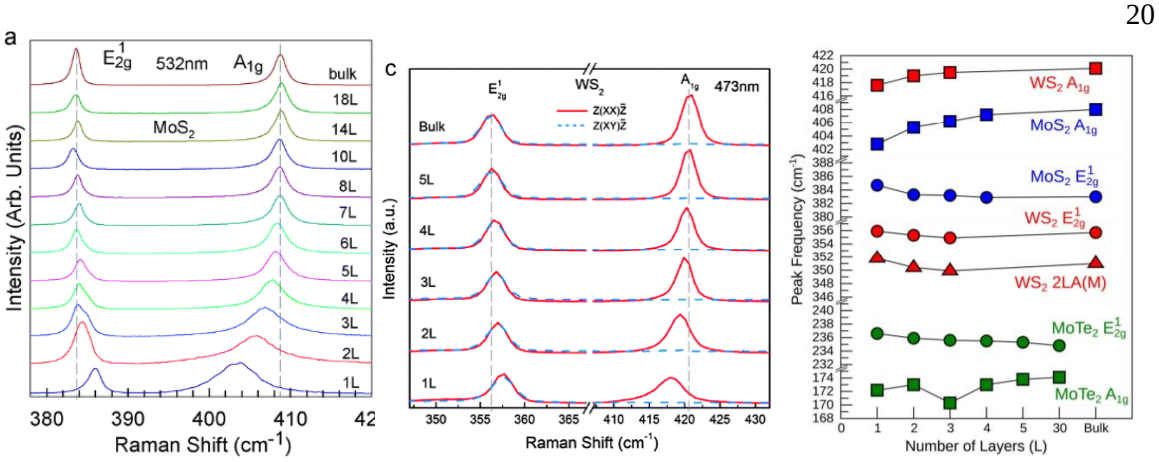

Figure 13: Raman spectra for MoS_2 (Left) and WS_2 (middle) for different layer numbers [39]; (Right) plot showing the effect of layer number on Raman mode peak positions for different TMDs [40].

Since WS_2 is the TMD studied in this work, more specific detail on its Raman features is provided in the following paragraphs and figures.

Previous research has identified three first order modes and a second order mode that are characteristic of the Raman of single and few layer WS_2. The $E^1_{2g}(\Gamma)$ mode, which is technically the E'(Γ) for an odd number of WS_2 because of a lack of inversion symmetry [41], is a first-order in-plane phonon mode that appears at the Brillouin zone center (Γ point). As seen in the right most plot of Figure 13, this mode shows a subtle redshift in WS_2 for an increasing number of layers [42].

The $A^1_{2g}(\Gamma)$ mode, which also is technically the $A_1'(\Gamma)$ mode for non-even numbers of layers [41], is a first-order out-of-plane phonon mode that appears at the Brillouin zone center. The intensity of this mode decreases with a decreasing number of layers, which previous research has suggested is due to dependence of this mode on interlayer coupling. With fewer layers, the phonon restoring forces associated with this mode, which are caused by van der Waals interactions between layers, are weakened, and hence the weakened Raman intensity [42].

As shown in the right most plot in Figure 13, this mode blueshifts for an increasing number of layers.

The LA(M) mode is a first-order longitudinal acoustic phonon mode that occurs at the Brillouin zone edge (M point) and is activated by disorder. The LA(M) mode, which describes in-plane collective oscillations of atoms in the lattice, is similar to a sound wave in that it is associated with the periodic compression and expansion of the lattice in the direction of propagation [42]. Mignuzzi et al. have correlated the intensity of LA(M) with the presence of defects in a sample [43].

The second order of LA(M), denoted as 2LA(M), is a resonant Raman feature that is particularly prevalent at an excitation of 514.5 nm in monolayer WS_2. In fact, the intensity of the 2LA(M) peak is about twice that of the A_1'(Γ) peak for monolayer WS_2 at the resonant excitation. The intensity of this peak increases for a decreased number of layers. As shown in the spectra in Figure 14, the 2LA(M) mode overlaps with the E'(Γ); Lorentzian fits (the red curves in Figure 14) are used to identify each individual peak. This second order mode is due to a double resonant Raman process, which requires two phonons with equal and opposite momentum. The process is termed double resonant because it involves an intermediate excited electronic state that resonates with the electronic band structure as well as a resonance for the initial optical transition. Like E'(Γ), 2LA(M) shows a subtle redshift for an increasing number of layers [42].

Overall, a comparison of Figure 14e and Figure 14f shows that with an excitation of 488 nm, the Raman spectrum of monolayer WS_2 is dominated by first-order features. At 514.5 nm, higher-order features, such as the resonant 2LA(M) mode, and combination modes become more prevalent. The inset of Figure 14f shows the atomic displacements for the E^1_{2g}(Γ) and the A^1_{2g}(Γ)

for two adjacent layers; the dashed line between layers represents the weak van der Waals interaction [42].

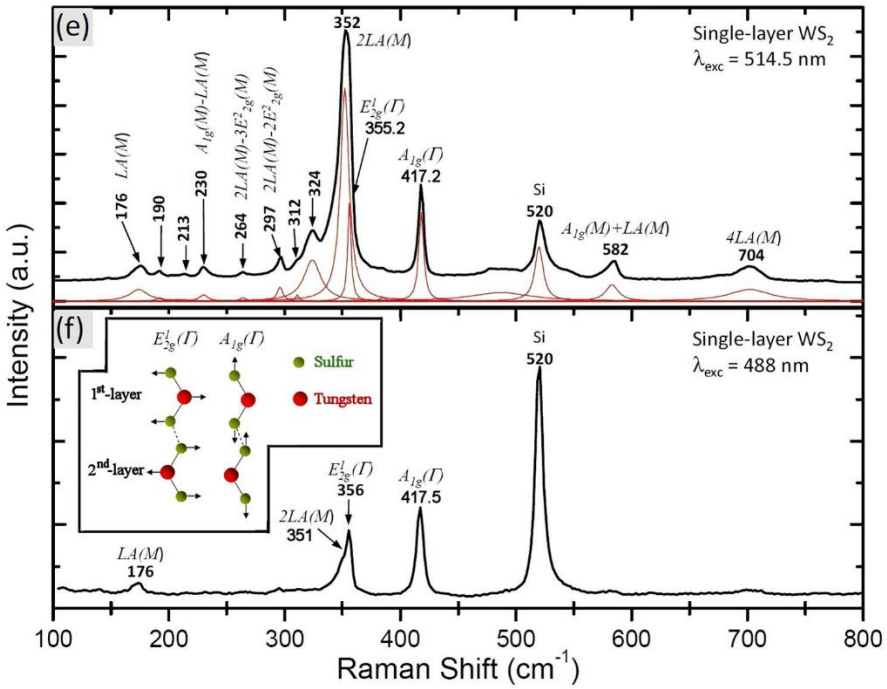

Figure 14: Raman spectrum of single layer WS_2 at 514.5 nm excitation (e) and a 488 nm excitation (f); the red curves shown in (e) are Lorentzian fits used to identify the contributions of individual peaks. The inset shown in (f) shows the atomic displacements for the $E^1_{2g}(\Gamma)$ and the $A^1_{2g}(\Gamma)$ for two adjacent layers, and the dashed line represents the weak van der Waals interaction between layers.

Surface Enhanced Raman Spectroscopy

Surface enhanced Raman spectroscopy (SERS) is a phenomenon in which the intensity of the Raman signal from molecules in proximity to a surface of certain finely divided metals is significantly enhanced. The SERS phenomenon was first observed by researchers at the University of Southampton's Department of Chemistry in 1973; the researchers observed a surprisingly strong Raman signal from pyridine adsorbed on a roughened silver electrode [44]. The weak intensity of Raman signal in conventional Raman spectroscopy limited its

applications, but the enhancement provided by SERS makes possible many more uses. Since its discovery in 1973, SERS has been employed in applications across many fields of research, including disease detection, the study of reactions at the single molecule level, food and water quality analysis, and other nanoscale sensing [45].

Mechanism

Despite the widespread use of SERS in research, there is still no consensus on the underlying mechanism of its signal enhancement [45]. In 1977, two separate theories for the SERS mechanism were proposed: an electromagnetic enhancement and a chemical enhancement [45]. More recently, chemical enhancement has been divided into three separate mechanisms. Jensen et al. identify these three chemical enhancement mechanisms as (a) a ground state chemical interaction between the metal nanoparticle and molecule (CHEM), (b) resonance Raman (resonance), and (c) charge transfer resonance Raman enhancement (CT) when the excitation wavelength is resonant with metal nanoparticle-molecule charge transfer transitions. Jensen et al. also attribute the mechanism of electromagnetic enhancement to a (d) strong localized field that exists when the plasmonic oscillations in the metal nanoparticle-molecule system are resonant with the excitation wavelength [46]. A schematic representing

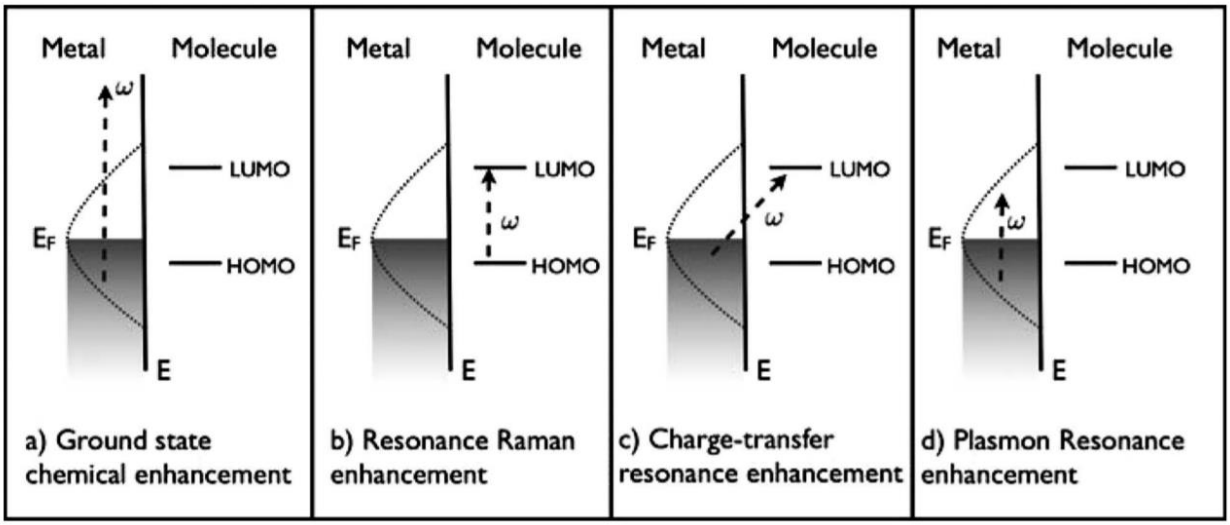

Figure 15: Energy level schematics for different Raman enhancement mechanisms for SERS, with ω corresponding to the excitation energy [43].

each of the four mechanisms, (a), (b), (c), and (d), that Jensen et al. describe is presented in Figure 15.

While the enhancement mechanisms are difficult to test and validate experimentally, a clearer understanding of the underlying mechanism would aid in more effective design of future SERS experiments and the development of applications. The following sections review literature which aimed to elucidate these mechanisms.

Chemical Enhancement—CHEM and Resonance Raman Mechanisms

In their review of computational electronic structure methods for studying SERS, Jensen et al. examine studies that investigate a Ag_{20}-pyridine complex (a common SERS system). Their findings are presented in Figure 16.

Comparing the spectra in Figure 16A with the bottom spectra shown in Figure 16C (both off-resonant conditions, or 514 nm excitations) isolates the CHEM contribution to the enhancement. All of the other three mechanisms require a resonance condition to be satisfied.

Jensen et al. note that the CHEM enhancement correlates with the induced polarizability, or the difference in the polarizability of the Ag_{20}-pyridine complex and the sum of the isolated silver cluster and the molecule. Thus, it can be deduced that the induced polarizability reflects the degree of chemical interaction between electronic states in the two systems [46].

The resonance Raman mechanism is closely tied with CT. In fact, CT often quenches the interfering fluorescence background, allowing for the resonance enhancement to manifest itself [46].

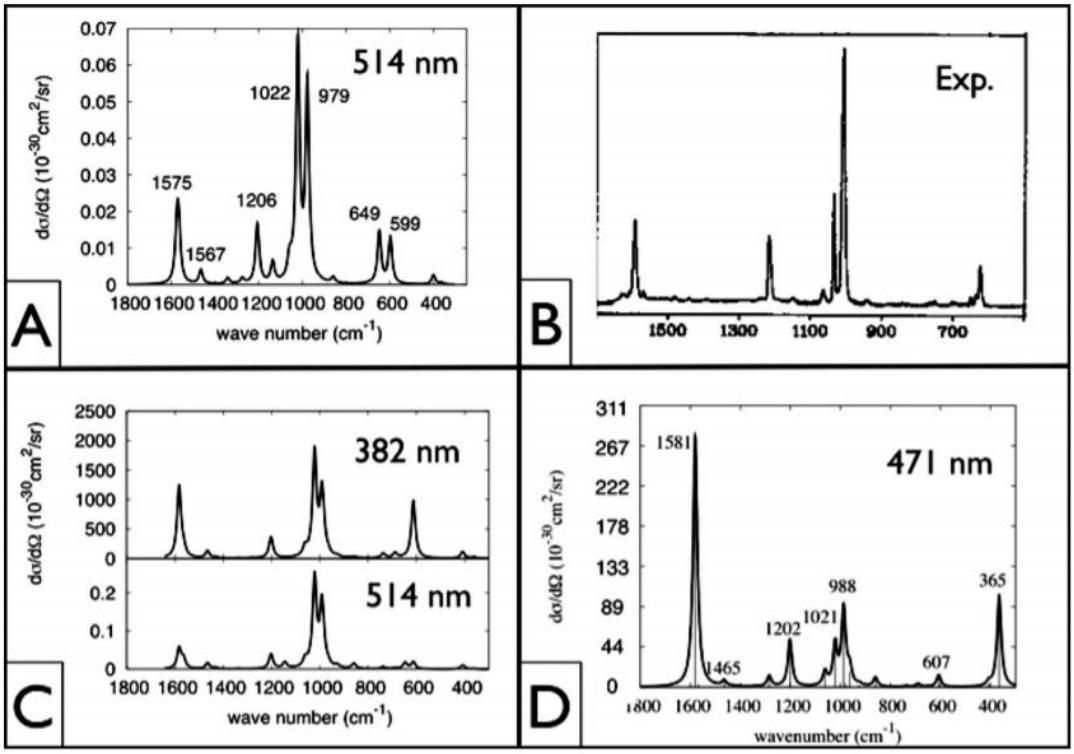

Figure 16: (A) Simulated normal Raman spectrum of pyridine at 514 nm; (B) experimental SERS spectra of Ag_{20}-pyridine SERS system; (C) simulated SERS spectrum of Ag_{20}-pyridine at 382 nm (top) and 514 nm (bottom); (D) simulated SERS spectrum of Ag_{20}-pyridine at 471 nm [43].

Chemical Enhancement—Charge Transfer Mechanism

The primary mechanism proposed for the chemical enhancement of Raman modes is the charge transfer (CT) mechanism. The chemical enhancement theory contends that the CT mechanism, an intermediate stage of the Raman resonance in which higher energy electrons in the substrate (surface) are transferred to the lower energy adsorbate, explains the increased signal intensity of the resulting Raman spectrum [47,48]. The following paragraphs review literature that have investigated the CT mechanism of SERS.

Yamada et al. investigated the effect of the CT band (a new spectral peak detected at ~600 nm after adsorption of pyridine) on the SERS mechanism in the pyridine-silver system. The researchers validated that the band was indeed due to CT and not due to an impurity. Furthermore, the excitation profile of the Raman spectra aligned with the CT band, but not the silver band, which also suggested that the enhancement was due predominantly to CT rather than an electromagnetic mechanism. They found that the stronger the CT band, the greater the SERS enhancement ($\sim 10^6$) [47]. From a comparison of the SERS intensity differences in annealed and unannealed silver, the researchers estimated that the electromagnetic signal enhancement in the system was $10\text{-}10^2$ while the CT enhancement was higher ($\sim 10^3$) [47].

Another paper published in 1994 by Osawa et al. studies SERS in p-aminothiophenothiol (PATP) adsorbed on silver [48]. The researchers showed that the presence of an electron transition from the ground state to the lowest occupied molecular orbital (LUMO) corresponds to the strong SERS bands. They assert that this electron transition to the LUMO is a result of the CT mechanism as the CT from the metal to the molecule occurs when charge is transferred from the Fermi level in the metal to the LUMO in the molecule [48]. Though they had started with a hypothesis relying on electromagnetic enhancement, the researchers discovered that the selective

enhancement of only four particular modes in the system could not be explained by the electromagnetic mechanism. They proceeded to investigate the intensity of the SERS bands as a function of applied potential, as shown in Figure 17.

In electrochemical environments, the intensity-potential profile shifts to positive potentials with an increase in excitation energy. This relationship corresponds to a Raman resonance associated with photon-induced CT from the metal to an affinity level in the adsorbate. Using ultraviolet resonance Raman spectroscopy (UVRR) as well as considering symmetry, they proved that this affinity level corresponds to the LUMO in PATP [48]. This paper not only demonstrates the presence of the CT mechanism in PATP-silver SERS, but also supports it by illustrating the strong relationship between intensity and applied potential. The researchers, however, caution that in most other SERS systems, a significant portion of the signal enhancement has not been attributed to the CT mechanism [48]. Thus, though it seems to explain this PATP-silver system, it is unlikely that the CT mechanism completely elucidates the enhancement provided by SERS. Yamada et al. and Osawa et al. offer compelling evidence for the existence of the CT mechanism, but not for CT being the primary mechanism for SERS across diverse systems.

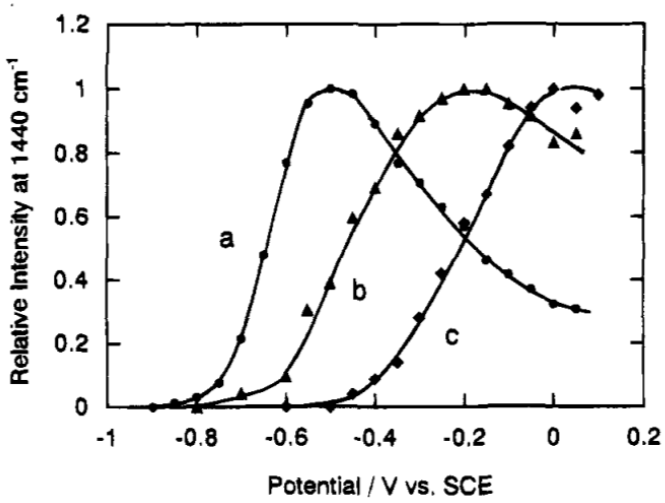

Figure 17: The plot shows the relationship between relative intensity and applied potential (against a saturated calomel electrode (SCE)) for the (a) 632.8-nm, (b) 514.5-nm, and (c) 488.0 nm excitations, observed by Osawa et al. The maximum intensities are shifted towards positive potentials for higher energy excitations [45].

Electromagnetic Enhancement

The electromagnetic enhancement can be explained by the excitation of localized surface plasmons. This theory contends that incident light excites surface plasmons in the metal surface, and when the light is resonant with the plasmon frequency, the electric field is enhanced, which thereby enhances the Raman signal. Plasmonic oscillations must be perpendicular to the surface to obtain this enhancement, and so roughened metal surfaces are often employed in SERS. For this electromagnetic mechanism, the total enhancement scales with $|E|^4$, where |E| is the electric field strength [46].

Jensen et al. review a study which simulated electromagnetic enhancement in Ag_{20}-pyridine complexes. The excitation wavelength used, 382 nm, is resonant with plasmonic oscillations in silver, and the result is shown in the top spectrum in Figure 16C in section 1.3.1.1.

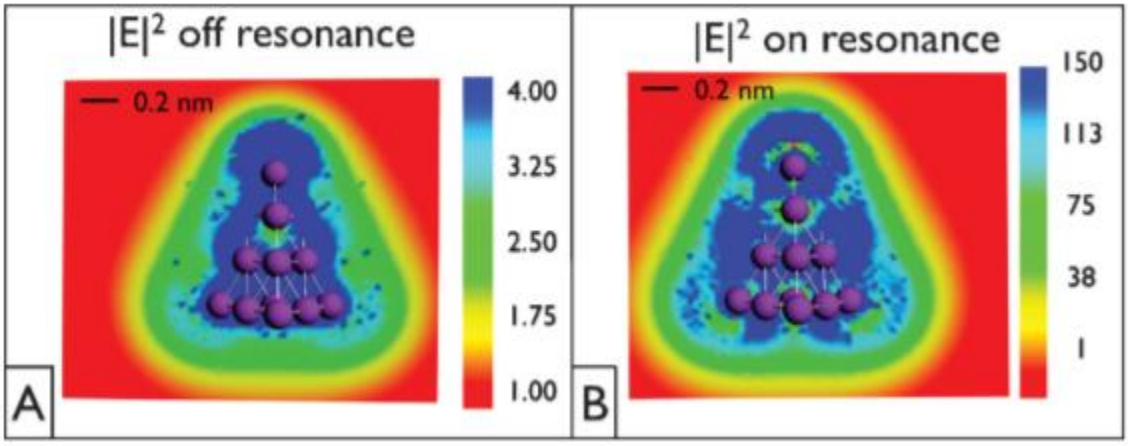

Figure 18: Simulated electric field distributions near Ag_{20} cluster for (A) off-resonant (514 nm) and (B) on-resonant (382 nm) excitation (382 nm is resonant with plasmonic oscillations in silver cluster) [43].

Figure 18 simulates the electric field distribution around a Ag_{20} cluster for the off-resonant (514 nm) excitation (A) and on-resonant excitation (382 nm) (B).

A much stronger local field distribution is shown in Figure 18B, which also corresponds to an excitation that provides a much greater SERS enhancement, as shown in the top spectrum of Figure 16C. Thus, the presence of a plasmonic "hotspot" correlates strongly with large enhancement from metallic SERS substrates. Furthermore, this theoretical simulation is corroborated by experimental results from many SERS systems, which show that electromagnetic enhancement from localized surface plasmon resonance is the most dominant mechanism for enhancement in SERS [46].

Brolo et al. investigated the effect of surface morphology on SERS in pyrazine adsorbed on gold. Using oxidation-reduction cycles, the surface roughness of the polycrystalline gold electrodes was controlled. The researchers found that the roughened gold surfaces showed far higher SERS intensities than "unroughened" gold electrodes [49]. Therefore, the research conducted by Brolo et al. gives support to the electromagnetic theory of SERS enhancement.

Furthermore, in recent papers, there has been an increase in the use of roughened surfaces for SERS, which suggests increased acceptance of the electromagnetic mechanism [45].

Another recent paper discussing plasmonics as a mechanism for SERS is a study by Yoshida et al. in 2009, which investigates SERS of chemical dyes adsorbed in gold nanoaggregates. The authors outline their theoretical calculations for the total emission cross-section spectra of Raman scattering; their calculations are based on the electromagnetic theory as they employ the amplitudes of the near and far electric field and electromagnetic enhancement factors. They show that their calculations produce very similar spectra to the experimentally collected plasmonic resonance spectra for R6G dye adsorbed on gold [50], as demonstrated in Figure 19.

The researchers acknowledge that their work does not deny the possibility of other sources of enhancement. For instance, the authors point out that exchanging one of the electromagnetic enhancement factors with a term that includes charge transfer in their calculations could account for the signal enhancement as well [50].

The development of newer SERS systems also sheds light on the SERS enhancement mechanism. For instance, Yang et al. developed slippery liquid-infused porous SERS (SLIPSERS), which employs a slippery, omniphobic substrate to concentrate analytes and SERS substrates within a droplet of organic liquid. The researchers show that this platform is capable of detecting at the single-molecule level. They found that this detection limit could be adjusted by tuning the geometries of the gold nanoparticles (SERS substrates). In particular, Yang et al. saw that tuning the size of the gaps between the gold nanoparticles adjusts the SERS signals; the strongest SERS signals from the analyte came from the molecules in these gaps [51]. The dependence of the SERS intensity on the geometry of the nanoparticles provides strong evidence

for the electromagnetic mechanism. Furthermore, the dependence on gap size and the fact that the strongest intensities exist in the gaps give even stronger support for this mechanism: these findings suggest the formation of SERS hotspots produced by plasmonic oscillations, which cause a strong magnetic field to form in the gaps [51].

The development of newer SERS systems also sheds light on the SERS enhancement mechanism. For instance, Yang et al. developed slippery liquid-infused porous SERS (SLIPSERS), which employs a slippery, omniphobic substrate to concentrate analytes and SERS substrates within a droplet of organic liquid. The researchers show that this platform is capable of detecting at the single-molecule level. They found that this detection limit could be adjusted by tuning the geometries of the gold nanoparticles (SERS substrates). In particular, Yang et al. saw that tuning the size of the gaps between the gold nanoparticles adjusts the SERS signals; the strongest SERS signals from the analyte came from the molecules in these gaps [51]. The dependence of the SERS intensity on the geometry of the nanoparticles provides strong evidence for the electromagnetic mechanism. Furthermore, the dependence on gap size and the fact that the strongest intensities exist in the gaps give even stronger support for this mechanism: these findings suggest the formation of SERS hotspots produced by plasmonic oscillations, which cause a strong magnetic field to form in the gaps [51].

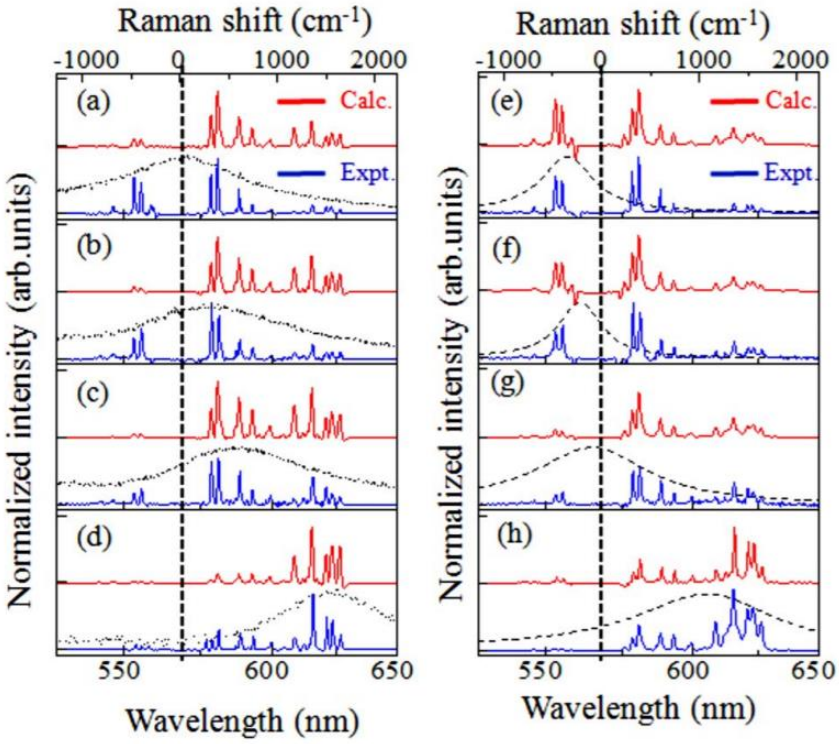

Figure 19: The plots show both experimental and calculated SERS spectra from Yoshida et al. The vertical offsets between the calculated and experimental spectra were added for the viewer to be able to distinguish between the spectra [47].

Enhanced Raman Spectroscopy with 2D Materials

Graphene enhanced Raman spectroscopy (GERS) is a special type of SERS that utilizes graphene as the enhancing substrate. Ling et al. were the first to observe Raman enhancement with graphene; they did so by adsorbing Raman probe molecules, phthalocyanine (PC), rhodamine 6G (R6G), protoporphyin IX (PPP), and crystal violet (CV), onto graphene on a Si/SiO_2 wafer. By comparing Raman measurements on bare Si/SiO_2 to those on graphene, Ling

et al. found that the peak intensities for PC molecules adsorbed on monolayer graphene were two to seventeen times greater [52].

Graphene Enhanced Raman Spectroscopy (GERS) Mechanism

Unlike many applications of SERS, GERS does not support the electromagnetic enhancement mechanism. This is because graphene is smooth unlike the roughened metal surfaces used in other forms of SERS, which allow for the propagation of plasmonic oscillations in the SERS substrate for electromagnetic enhancement. Furthermore, graphene's surface plasmon resonance occurs in the terahertz region while the excitation laser wavelengths used to probe graphene in Raman measurements are in the visible range [10,53].

The mechanism assigned to the enhancement in GERS is the chemical enhancement mechanism, and the primary mechanism proposed for this chemical enhancement of Raman modes is charge transfer (CT). The chemical enhancement theory contends that the CT mechanism, an intermediate stage of the Raman resonance in which higher energy electrons in the substrate (surface) are transferred to the lower energy adsorbate, or vice versa, explains the increased signal intensity of the resulting Raman spectrum [1,53].

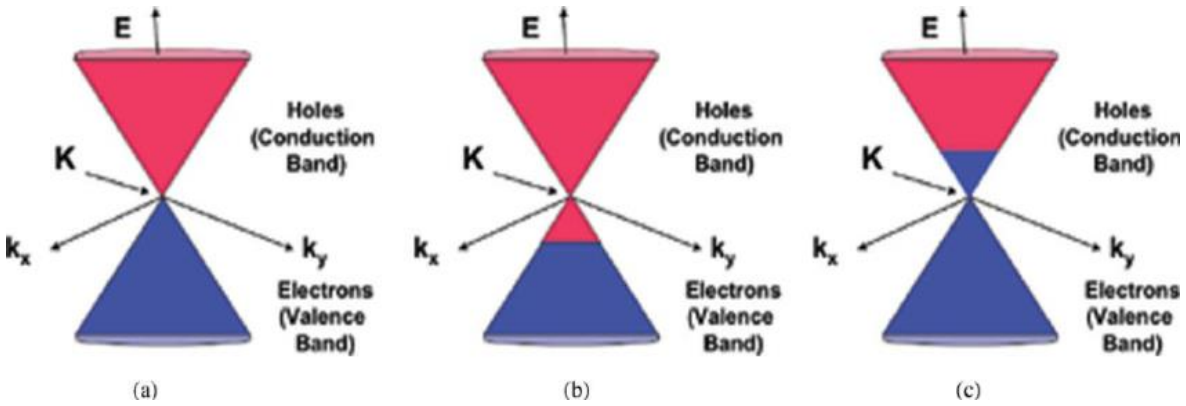

Figure 20: (a) Undoped graphene, (b) graphene doped with extra holes (e.g. boron doped graphene), and (c) graphene doped with extra electrons (e.g. nitrogen doped graphene) [51].

Numerous studies have attempted to elucidate the CT mechanism in graphene from different perspectives. Recent research on GERS have showed that the alignment of the LUMO of the molecule with the Fermi level of graphene allows for supposed enhanced CT, and thereby amplification of the molecule's vibrational modes. To enable better LUMO-Fermi level alignment between the molecule and graphene substrate, researchers have proposed doping graphene. For instance, doping graphene with extra electrons (e.g. nitrogen) shifts the Fermi level up into the conduction band, whereas doping with extra holes (e.g. boron) shifts the Fermi level down into the valence band (see Figure 20) [54]. Therefore, controlled doping could be used to tune the position of the Fermi level in graphene to match the LUMO of the molecule. By using a laser excitation slightly larger than the HOMO-LUMO gap of the molecules to be analyzed (slightly larger than the gap to account for energy loss), a resonance condition can be achieved, allowing for further enhancement of the molecules' Raman spectra.

Still, more clarity on the enhancement mechanism in graphene and other 2D materials used as Raman enhancing substrates is necessary. The following paragraphs form a brief historical overview of work that has investigated the Raman enhancing capabilities of 2D materials since Ling et al.'s discovery of GERS in 2010.

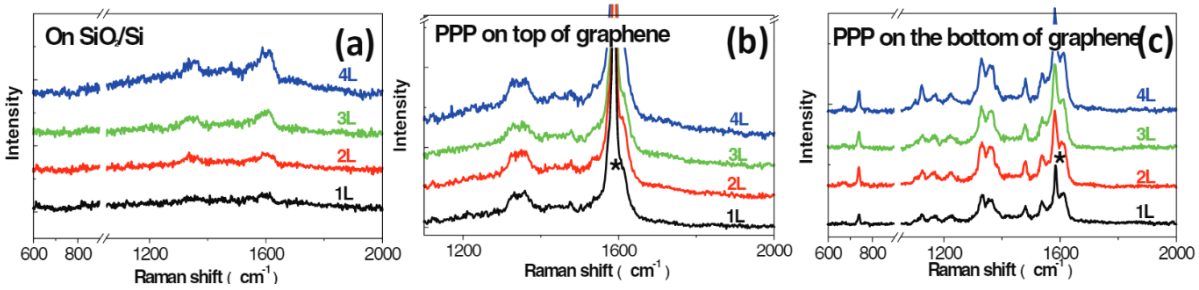

Figure 21: These graphs show Raman spectra of PPP without GERS enhancement (a), with GERS enhancement and PPP on top (b), and with GERS enhancement and PPP on the bottom (c). Plots (b) and (c) illustrate the first layer effect because the difference in intensity between the first layer of PPP and subsequent layers is negligible [50].

Ling and Zhang studied the "first layer effect" in GERS. The first layer effect is based on the idea that the first layer of the adsorbed molecule chemically interacts with the substrate and contributes most dominantly to the Raman enhancement. This effect gives evidence for CT in GERS (for CT to occur, the molecule needs to be in contact, or in very short range, with the substrate) [53]. To determine whether the first layer effect was present in GERS, Ling and Zhang transferred graphene onto a silicon-silicon dioxide substrate and transferred Langmuir-Blodgett films of protoporphyrin IX (PPP) layer by layer such that the PPP film was in contact with the graphene (either underneath or above the graphene). They investigated the effect of adding layers of PPP films on the Raman intensity and found that there is very little difference in the enhancement after the first monolayer of PPP (see Figure 21) [53]. These results corroborate the first layer effect, which in turn supports the CT mechanism in GERS. Furthermore, the researchers replicate the effect with PPP both on top of the graphene and below the graphene [53]. These results validate their argument that the determining factor for the enhancement is the contact between the PPP and the graphene and further bolster the CT mechanism for GERS.

Huang et al. offered selection rules for molecules that could be enhanced by GERS. These rules were based on energy levels as well as structural symmetry of the molecules relative to graphene. By obtaining GERS spectra of three molecules that are structurally very similar, CuPc, ZnPc, and F_{16}CuPc (all with D_{4h} symmetry), but with different energy-level (HOMO/LUMO) gaps (−5.2/−3.5 eV, −5.2/−3.8 eV, and −6.3/−4.8 eV for CuPc, ZnPc, and F_{16}CuPc, respectively), Huang et al. found that the GERS enhancement of the same vibrational mode (at the same laser excitation wavelength (633 nm)) to be 3.8 and 7.6 times larger in CuPc than in ZnPc, and F_{16}CuPc, respectively. These experimental results suggest that the HOMO/LUMO energies of the molecules have an important role in GERS enhancement (see Figure 22) [55]. They use their experimental results along with theoretical predictions from Barros et al. to suggest an "energy level selection rule." Barros et al. use time-dependent perturbation theory for Raman scattering processes to derive four equations, (equations (i), (ii), (iii), and (iv)), conditions, which when satisfied, achieve a large GERS enhancement (ħ is Planck's reduced constant, ω_0 is the laser excitation frequency, $LUMO$ is the energy level of the lowest unoccupied molecular orbital in the analyte, $HOMO$ is the energy level of the highest occupied molecular orbital in the analyte, E_F is Fermi energy in graphene, and ω_q is the phonon frequency) [56]:

$$(i)\ \hbar\omega_0 = LUMO - HOMO\ or\ \hbar\omega_0 = LUMO - HOMO + \hbar\omega_q$$

$$(ii)\ E_F = HOMO \pm \hbar\omega_q\ or\ E_F = LUMO \pm \hbar\omega_q$$

$$(iii)\ \hbar\omega_0 = E_F - HOMO\ or\ \hbar\omega_0 = E_F - HOMO + \hbar\omega_q$$

$$(iv)\ \hbar\omega_0 = LUMO - E_F\ or\ \hbar\omega_0 = LUMO - E_F - \hbar\omega_q$$

Summarizing equations (i) through (iv) suggests that when the phonon energy is close to the energy difference between the graphene Fermi energy and the HOMO/LUMO level of the

molecules, GERS enhancement will be strong. Moreover, under this condition, the GERS enhancement can be further increased by matching the incident laser energy with the HOMO/LUMO gap of the molecule (resonance Raman) [55,56]. The experimental results presented by Huang et al. mostly corroborate Barros et al.'s theoretical predictions. They find that the GERS enhancement for CuPc increases with phonon frequency up to the resonance condition (equation (ii)). However, Huang et al. find that the energy level selection rule is less successful in explaining enhancement in molecules of different structures. To investigate the role of molecular structure in GERS enhancement, Huang et al. adsorbed three molecules, TTP, TCTA, and sp2-NPB, with similar HOMO-LUMO gaps (-5.5eV/-2.4eV, -5.7eV/-2.4eV, and -5.6/-2.3eV, respectively), but with different molecular symmetries, D_{2h}, C_3, and S_4, respectively, onto monolayer graphene and compared GERS spectra (see Figure 23). They found that the enhancement of the mode at 1450 cm^{-1} under a 633 nm excitation for TTP is about 3.4 and 5.4 times that of TCTA and sp2-NPB, respectively. Since, there is relatively no difference in the HOMO/LUMO gaps of these molecules, Huang et al. suggest that the difference in enhancement is due to the degree in similarity of the symmetry of the molecules to graphene ($D_{2h} > C_3 > S_4$ in terms of matching the D_{6h} symmetry of graphene). This similarity in symmetry strengthens the molecule-graphene coupling, the van der Waals interaction between the graphene and the molecule, which is correlated with a higher GERS enhancement according to the perturbation theory of Raman scattering [55].

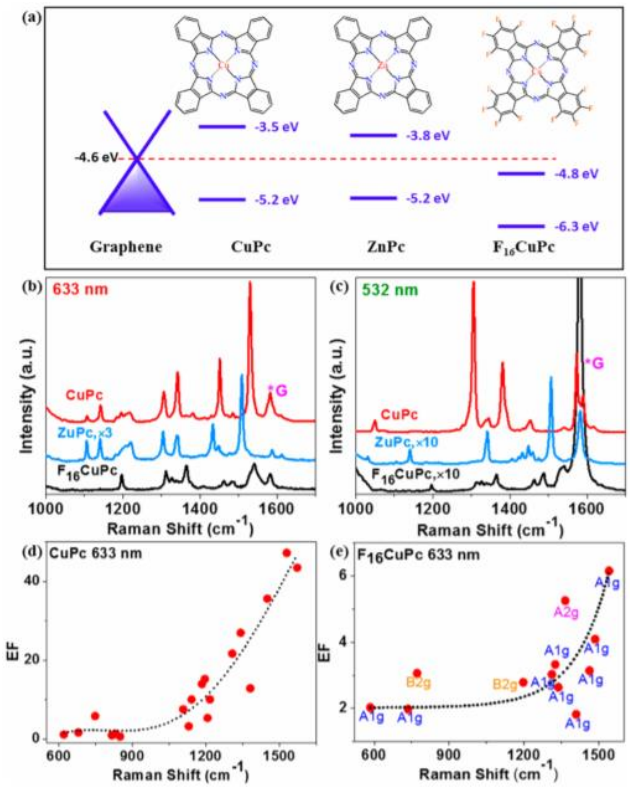

Figure 22: For molecules of similar symmetry and different energy levels: (a) energy level diagrams, enhanced Raman spectra with (b) 633nm and (c) 532nm excitations, respectively, and enhancement factors versus Raman shift for (d) 633nm and (e) 532nm excitations, respectively [52].

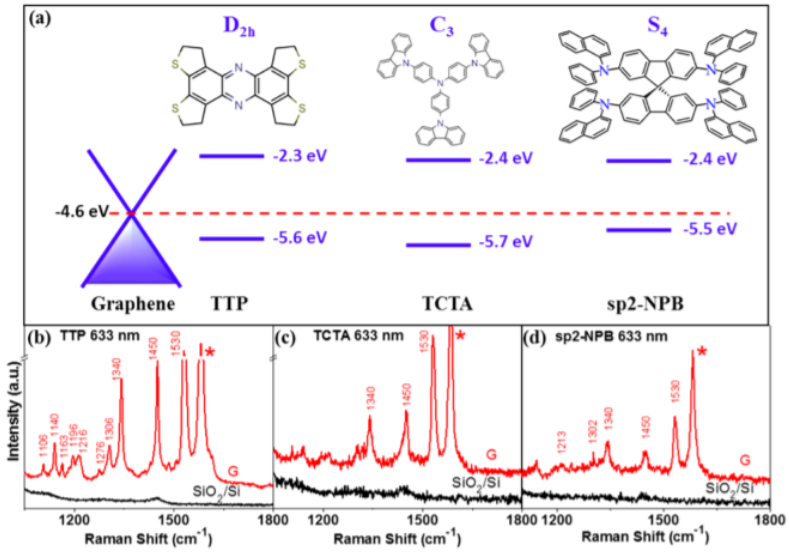

Figure 23: (a) Energy level diagrams of molecules with similar energy levels but different symmetries; (b), (c), and (d) show enhanced Raman spectra of the three molecules on graphene [52].

Variations on Conventional GERS: Other 2D Materials, Hybrid Structures, etc.

In addition to pristine graphene (PG), the Raman enhancement capabilities of other two-dimensional substrates have been investigated. Various doped graphene variants of GERS have been studied. For instance, Feng, et al. have shown that nitrogen-doped graphene (NG) enhanced the Raman signal of dye molecules via GERS. They present GERS spectra of three different molecules, rhodamine B (RhB), crystal violet (CrV), and methylene blue (MB), comparing the enhancements of these molecules on NG to those on PG and bare Si/SiO_2 substrates. The Raman signal from these dyes (at their corresponding resonant excitation lines) on bare Si/SiO_2 is invisible due to the strong fluorescence background of these molecules. Obtaining Raman spectra of these dyes on NG quenches the fluorescent background and enhances the Raman signal [1]; this is believed to be due to the charge transfer between NG and the adsorbate, which disrupts the recombination of electron-hole pairs in the adsorbate—and thereby the fluorescent background [1,57]. Thus, it is clear that the Raman enhancement is not just due to resonance Raman, but also due to the NG substrate. This can also be corroborated from examining Feng et al.'s GERS spectra for the three dyes at different laser excitations. Though the enhancement of the dyes' spectra is the best in the case of resonance Raman (when the laser excitation matches the HOMO/LUMO gap of the dye; this corresponds to 2.41eV for RhB and CRV and 1.92eV for MB), some features of the dyes (those not corresponding to the graphene D, G, and 2D peaks) are still visible for non-resonant excitations due to the enhancement from NG (see Figure 24) [1].

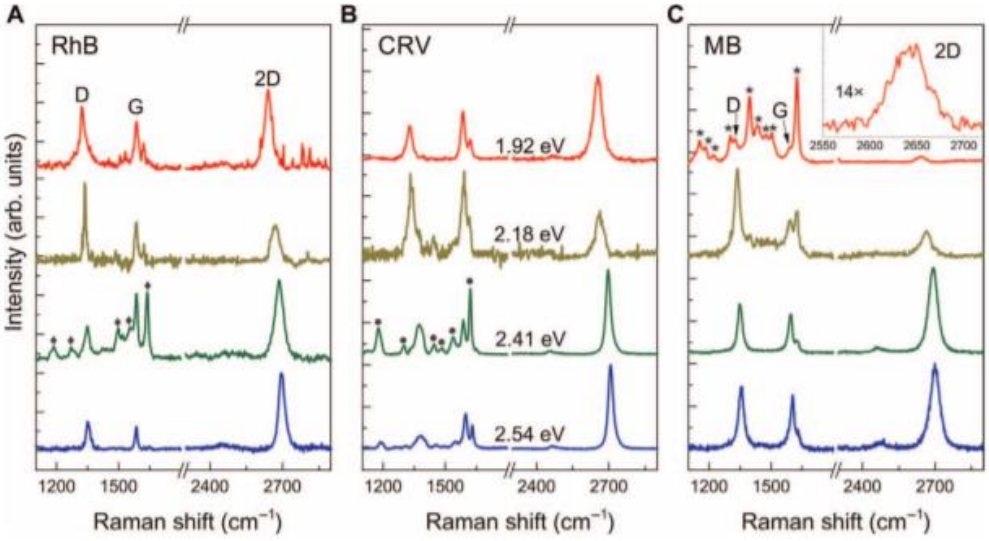

Figure 24: NG enhanced Raman spectra of (A) RhB, (B) CRV, and (C) MB [1].

Feng et al. further characterized the Raman enhancement for NG based GERS versus that for PG and SERS (gold nanoparticles) and found that the NG enhancement was 5 and 10 times greater, respectively (see Figure 25) [1].

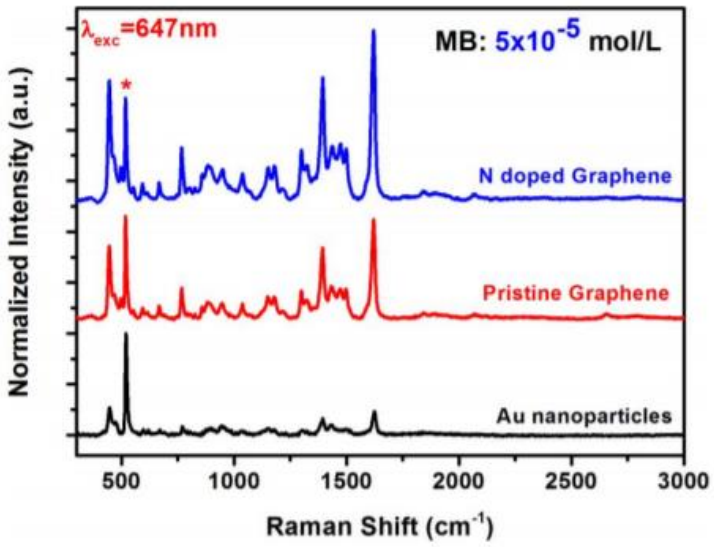

Figure 25: Enhanced Raman spectra of MB on NG, PG, and Au nanoparticles [1].

Unlike the previous work by Huang et al. on PG, Feng et al. found no correlation between symmetry and enhancement for NG based GERS. In fact, the dye which showed the

greatest enhancement, RhB, corresponded to the lowest symmetry correlation with graphene. Feng et al. combined their experimental results with density functional theory modeling to better understand NG based GERS and propose a mechanism for the enhancement based on energy levels. In this work, the dyes are cations that can be thought of as inducing image charges on graphene. The electric field of the image charges decrease the HOMO/LUMO gaps in the molecule. Feng et al.'s ab initio calculations suggest that the closer the LUMO in the analyte is to the Fermi level in the graphene surface, the greater the CT—and thereby, the greater the GERS enhancement. In theory then, the combination of the Fermi level movement into the conduction band from nitrogen-doping and the movement of the molecule's energy levels from the image charge electric field can explain the higher GERS enhancement seen in NG compared to that in PG [1].

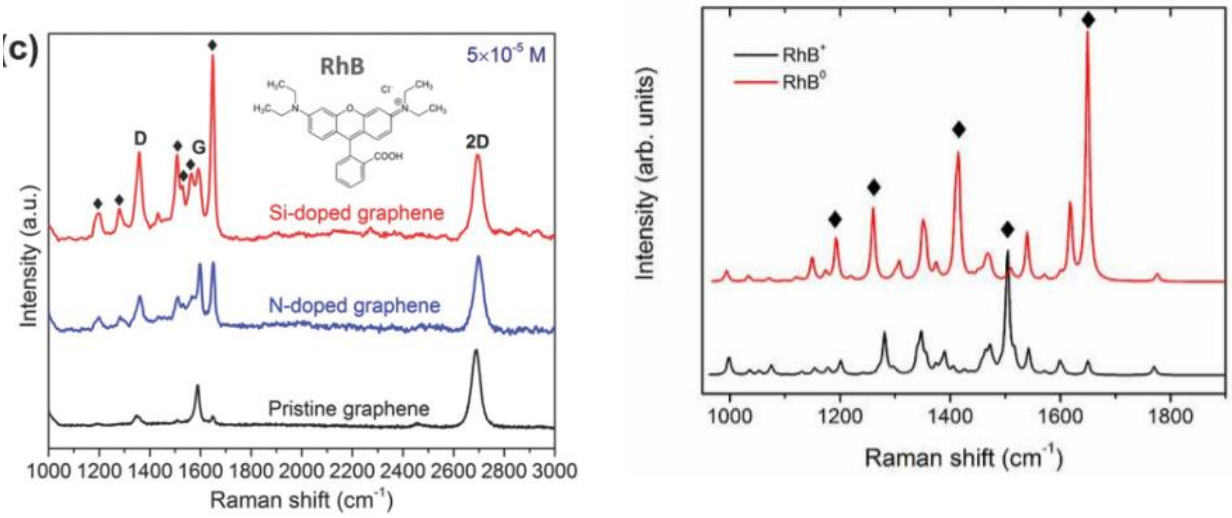

Figure 26: (Left) Enhanced Raman spectra of RhB on Si-doped graphene, NG, and PG; (Right) Theoretical raman spectra of RhB^+ and RhB^0 from DFT calculations [13].

An earlier work from Lv et al. agrees with Feng et al. in asserting that the proximity of the molecule's LUMO to the graphene (or doped graphene) Fermi level is important for enhanced Raman signals. However, experiments reported by Lv. et al show that the Si doped

graphene enhance the Raman spectra of RhB, CrV, and MB better than NG or PG. They suggest that this finding may be due to the stronger interaction between the adsorbates and the Si dopant compared to that between the adsorbates and nitrogen dopants or the carbon in pristine graphene. Furthermore, the study proposes that mechanism for enhancement could be viewed as an electronic excitation of graphene that is transferred to the dye; they perform a density functional theory analysis and show that the resulting Raman spectra of RhB could be interpreted as a mixture of RhB^{+} and RhB^{0}, which indicates some electronic transfer from graphene (or doped graphene) to the dye (RhB is a cation) (see Figure 26) [13].

Other works show that gas molecules, such as NO_2, could bind well to boron dopants in graphene and enhance its sensing capability [9]. However, there are no convincing studies on the enhanced Raman spectroscopy of boron doped graphene.

Because their electronic and surface chemical properties differ from graphene, hexagonal boron nitride (h-BN) and monolayer transition metal dichalcogenides (TMDs) are ideal candidates for further investigation of the Raman enhancement capabilities of 2D materials. Ling et al. studied the Raman enhancement of CuPc on pristine graphene, h-BN, and monolayer MoS_2 (see Figure 27). They identify two mechanisms contributing to the chemical enhancement of Raman modes: charge transfer and dipole-dipole interactions. Graphene, comprised of nonpolar C-C bonds, has weak dipole-dipole interactions with the adsorbate. However, graphene is a zero-bandgap semimetal, and when graphene comes in contact with CuPc, it increases the number of available electron states near the HOMO and LUMO of CuPc. According to Fermi's golden rule, the increase in the density of states increases the electron transition probability via charge transfer. Conversely, h-BN is an insulator with a bandgap of 5.9eV, and therefore, the density of states contributes very few available states for a charge transfer interaction with CuPc. However,

B and N form a strong polar bond, which can induce an interface dipole interaction with CuPc. This dipole interaction causes a local symmetry perturbation, which also increases the electron transition probability by Fermi's golden rule. Of the three species studied, MoS_2 had the weakest enhancement capability as it had weak charge transfer and dipole-dipole interactions with CuPc; MoS_2 is semiconducting with a band gap (not quite as many available electronic states as graphene) and not quite as polar as h-BN. Also, some of the CuPc peaks are covered up when adsorbed on an MoS_2 substrate due to the MoS_2 photoluminescence background. Higher frequency phonon modes tend to favor charge transfer, or in other words, are better enhanced on graphene than h-BN. Modes with larger dipoles are better enhanced by h-BN; in this study, the lower frequency phonon modes were better enhanced on h-BN than on graphene. Another interesting finding of this study is that the number of layers of h-BN has no effect on its enhancement factor because it is transparent in the visible range. This is unlike graphene: the enhancement factor of graphene decreases with increasing thickness. Ling et al. report that each additional layer of graphene absorbs 2.3% of the incident laser light [2].

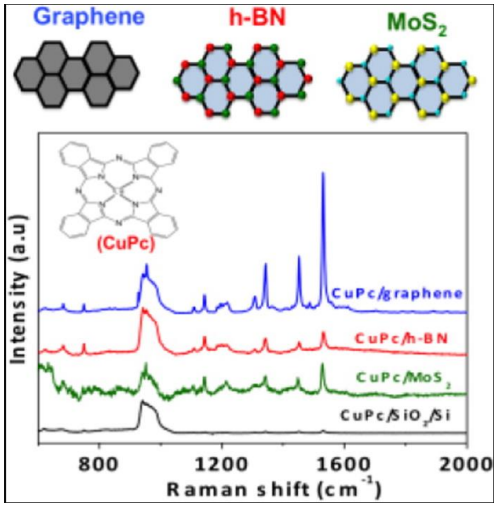

Figure 27: Enhanced Raman spectra of CuPc on graphene, monolayer h-BN, and monolayer MoS_2 [2].

Muehlethaler et al. observed enhanced Raman spectra (>3*10^5 enhancement) for 4-mercaptopyridine (4-MPy) when adsorbed on MoS_2 monolayers. The authors attributed this strong enhancement to the excitonic resonance of these semiconductors; it is explained that the enhancement is due to the laser excitation (488 nm) being in resonance with the charge transfer transitions (467 nm) and close to the shifted C-exciton resonance (360 to 390 nm). The authors further explain that the strong enhancement can be thought to result from vibronic coupling between the excitonic bands and those involved in the CT from the valence band of MoS_2 to unoccupied π^* orbitals in 4-MPy [58]. Liu et al. further the research on TMDs by demonstrating that the coupling of the exciton and charge transfer resonances can be tuned by adjusting the atomic ratio of W and Se in WSe_2 monolayers. This tuning can be accomplished by using ion irradiation to sputter or displace atoms from the crystal. They find that an Se:W ratio of 1.96 enhances the Raman spectra of CuPc better than pristine WeS_2 by more than 40 times [59].

A strategy employed to improve the electronic properties of 2D material Raman-enhancing substrates is oxygen or plasma treatment, which introduces surface defects and alters the band alignment between the substrate and the adsorbate. After UV/ozone-based oxygen treatment of pristine graphene, Huh et al. reported an enhancement of ~10^4, which was higher than the ~10^3 reported for untreated pristine graphene for the 1648 cm^{-1} mode in RhB. The authors attributed this greater Raman enhancement to higher surface polarizability, which allowed for greater molecule-graphene interaction and better band alignment for CT (because the oxygen-containing groups induce p-type doping in graphene) [60]. Sun et al. reported that treatment of MoS_2 with oxygen and argon plasmas increased the Raman enhancement of R6G. Similar to Huh et al.'s study on graphene, Sun et al. attributed the increased Raman enhancement

to p-type doping from oxygen adsorption and the induction of localized dipoles that enabled surface interaction between the MoS_2 and R6G [61].

Recently, attention has been given to hybrid plasmonic metal-2D material structures as SERS substrates. The addition of a monolayer to the plasmonic metal keeps the metal from oxidizing. For an Ag nanoparticle/h-BN hybrid substrate, the oxidative stability was maintained for over 80 days and a detection limit for R6G was established as low as 10^{-12} M [62]. However, the chemical enhancement mechanism contributes very little to the Raman enhancement from this SERS substrate; the dominant mechanism is electromagnetic.

Chapter 3

Methodology

Thus far, the predominant accepted mechanism of Raman enhancement on 2D material substrates is charge transfer. In previous research, Feng et al. have asserted that the proximity of the Fermi level in the 2D material to the LUMO of the adsorbate enhances this charge transfer. Furthermore, when the 2D material-adsorbate system is probed using laser excitations corresponding to the HOMO-LUMO gap of the adsorbate (resonance Raman), further enhancement is seen. Figure 28 and Figure 29 are schematics that summarize the proposed Raman enhancement mechanisms on graphene and WS_2 substrates, respectively.

To test this hypothesis, 2D materials with different Fermi level positions, monolayer WS_2 and monolayer graphene, were studied. Common chemical dyes, crystal violet, rhodamine 6G, and rhodamine B, were adsorbed on these 2D materials substrates to test their ability to enhance the Raman spectra of the dyes. For a given dye, results illustrating that its Raman spectrum was better enhanced by the 2D material substrate with a Fermi level closer to a dye's LUMO supported the hypothesis.

Figure 30 shows the Fermi level positions of monolayer WS_2, monolayer MoS_2, and monolayer graphene along with the HOMO/LUMO positions of CV, R6G, and RhB relative to vacuum level. These values were compiled from different theoretical and experimental studies in literature. Though experiments with monolayer MoS_2 substrates were not carried out in this study, its Fermi energy is plotted in Figure 30 for completeness. From the data collected in

Figure 30, it is clear that the Fermi level of monolayer WS_2 (E_F = -3.0 eV), is closer to the LUMO energies of rhodamine 6G and rhodamine B (LUMO = -3.40 eV and -2.73 eV, respectively) than the Fermi level of monolayer graphene (E_F = -4.6 eV). Also, graphene's Fermi energy is closer to the LUMO of crystal violet (LUMO = -4.10 eV) than is the Fermi energy of WS_2. Thus, it was expected that monolayer WS_2 would better enhance the Raman spectra of R6G and RhB while graphene would better enhance the Raman spectra of CV. Furthermore, it is predicted that using a laser excitation that matches the HOMO-LUMO gap of the dye, (1.90 eV (red laser) for CV, 2.30 eV (green laser) for R6G, and 2.24 eV (green laser) for RhB as shown in Figure 30) would allow for even greater enhancement via the resonant Raman mechanism.

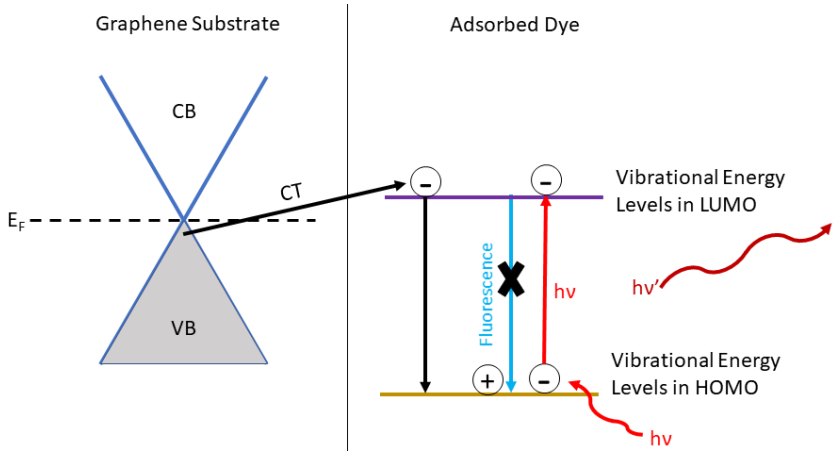

Figure 28: Schematic of enhancement mechanism in GERS: the dye molecule is adsorbed on the graphene substrate and the dye-substrate system is resonantly excited by a laser energy, hν, approximately corresponding to the HOMO-LUMO gap: due to the proximity of graphene's Fermi energy (E_F) to the dye's LUMO, charge is easily transferred from graphene to the dye; the resonant excitation excites electrons from the HOMO to the LUMO, leaving behind holes in the HOMO. The charge transfer process (represented by the black arrows in the schematic) is much faster than the relaxation of electrons from the LUMO to HOMO; thus, excited electrons in the dye are prevented from recombining with holes, and fluorescence (denoted by the light blue arrow) is quenched, or suppressed. Due to interactions with phonons in the dye, the outgoing light is of energy hν' where hν'<hν (Stokes Raman scattering).

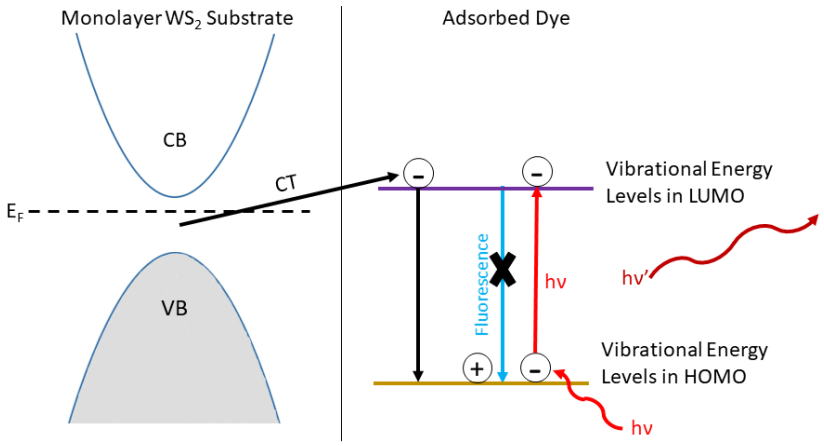

Figure 29: Schematic of enhancement mechanism in SERS with a WS_2 substrate: our hypothesis is that the mechanism is founded on CT from the substrate to the dye and that, just like the proposed GERS mechanism, the proximity of the E_F in WS_2 to the LUMO of the dye provides significant Raman enhancement under a resonant excitation.

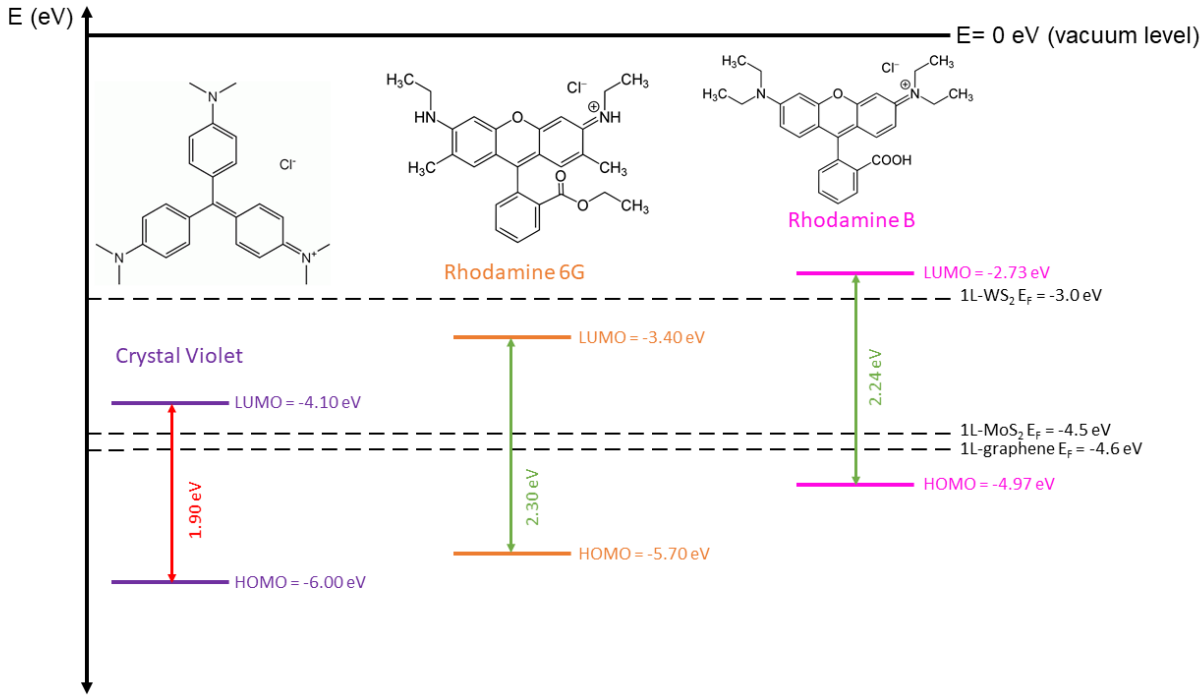

Figure 30: Theoretical energy-level alignment between 2D substrates and dyes: theoretical values for energy levels are obtained from literature (Fermi level for graphene and HOMO-LUMO for R6G and CV [52,63], HOMO-LUMO for RhB [64], Fermi levels for WS_2 [65] and MoS_2 [66]). The Fermi energy of WS_2 is closer to the LUMOs of RhB and R6G than is the Fermi energy of graphene; thus, we expect better CT to R6G and RhB and better Raman enhancement of R6G and RhB adsorbed on WS_2 than on graphene. Similarly, we expect better Raman enhancement for CV adsorbed on graphene than on a WS_2 substrate.

Chapter 4

Experimental Methods

Chemical Vapor Deposition Synthesis of Graphene

Graphene was synthesized by atmospheric chemical vapor deposition (APCVD) on Cu foil substrates and with a methane gas precursor. Two sets of synthesis parameters, referred to as method 1 and method 2; they are detailed separately in the following paragraphs.

In method 1, methane gas and flowed into the system at 15 SCCM during the synthesis and argon and 85% Ar-15% H_2 carrier gases were flowed into the system at 0.73 L/min and 0.33 L/min for all stages of the process (ramping up to synthesis temperature, annealing, synthesis, and cooling down). Before the synthesis, the substrate was annealed in the furnace for an hour at the growth temperature, 1000 degrees centigrade, to promote the growth of larger grains. During the synthesis, methane was introduced into the system for 30 minutes to allow for the adsorption and desorption of carbon from the Cu substrate. After the synthesis, the furnace was programmed to gradually cool down—stopping the temperature at 850 degrees centigrade; this seemed to help with obtaining higher quality monolayer graphene.

In method 2, graphene was also grown on Cu foil substrates using APCVD. Before the synthesis, the furnace temperature was ramped up to 1020 ºC in 30 minutes and subsequently to 1072 ºC in the next 30 minutes. The substrate was then annealed in the furnace at 1072 ºC for one hour to promote the growth of larger grains. During the ramping and annealing stages, argon and argon-hydrogen (85% Ar-15% H_2) carrier gases were flowed through the furnace at 600 SCCM and 400 SCCM, respectively. During the synthesis, the carbon containing precursor, methane gas, was introduced into the system at 1 SCCM for five minutes, and the argon and

argon-hydrogen carrier gases were also flowed into the system at 2000 SCCM and 667 SCCM, respectively. After five minutes, the furnace was switched off, but the gases continued to be flowed in to system. A 19/32 spanner was placed between the top cover and bottom cover of the furnace, and a desk fan was also switched on to aid in the cooling process. When the actual temperature on the furnace read 1000 ºC, the methane gas flow was turned off, and the argon and argon-hydrogen flow rates were reduced to those used during ramping and annealing. Finally, at 750 ºC, the furnace was fully opened to speed up cooling. When the temperature reading on the furnace reached room temperature, it was safe to take out the growth tube and remove the sample.

Graphene Transfer

Graphene samples were transferred from Cu foil to SiO_2/Si substrates for Raman experiments using a standard wet transfer process. PMMA was spin-coated onto the sample to protect the graphene while the copper foil was etched in an iron chloride bath. The graphene was subsequently transferred to a series of water baths, then transferred to the silicon substrate, and placed on a hot plate at 50 degrees centigrade to dry. After the transfer, PMMA was lifted-off by soaking the sample in acetone.

Atmospheric Pressure Chemical Vapor Deposition Synthesis of Monolayer WS_2

Monolayer WS_2 was grown directly on a Si/SiO_2 substrate in two CVD furnaces placed side by side. A crucible filled with sulfur powder was placed at the center of the first furnace; another crucible filled with WO_3 powder was placed at the center of the second furnace along

with the silicon substrate. For the synthesis, the first furnace was heated to 220 ºC and the second furnace was heated to 800 ºC. The synthesis was carried out for 15 minutes with a 1000 SCCM argon gas flow into the system.

Raman Spectroscopy for Characterizing Graphene and WS_2

Raman spectra were collected under ambient conditions using a Renishaw inVia micro Raman spectrometer and a Horiba (get exact name) spectrometer. For characterization of graphene samples with the Renishaw instrument, a 488nm solid state laser was used for the excitation. A 533 nm laser excitation was used for characterizing both pristine graphene and pristine monolayer WS_2 samples with the Horiba instrument. For WS_2, it was important to avoid photoluminescent background while doing Raman.

Enhanced Raman Spectroscopy Measurements on Chemical Dyes

Chemical dye solutions, crystal violet (CV), rhodamine B (RhB), and rhodamine 6G (R6G), were prepared by dissolving powders in ethanol. Powders were weighed out carefully using a mass balance, and serial dilutions were carried out to reach the desired concentration. The original (undiluted) dye solutions were prepared at 10^{-3} M, which required 20 mL of ethanol to be mixed with the appropriate mass of the dye (8 mg for CV and 9.5 mg for RhB and R6G).

Dye solutions were adsorbed onto 2D material substrates by soaking the substrates in the dye overnight. Raman measurements were made under ambient conditions using the Horiba (get exact name) spectrometer. When possible, the appropriate wavelength laser was chosen such that energy of the laser corresponded to the HOMO-LUMO gap of the molecule to be detected. An

open source MATLAB function [67] was used to subtract baseline noise from the spectra via Savitzky-Golay filtering.

Chapter 5

Results

Data

2D Material Samples

The 2D material substrates tested were WS_2 and pristine graphene, both synthesized via APCVD. Figure 31 is an optical microscope image of representative CVD grown pristine WS_2 triangles on a Si/SiO_2 substrate. The triangles shown are of monolayer or few layer regions.

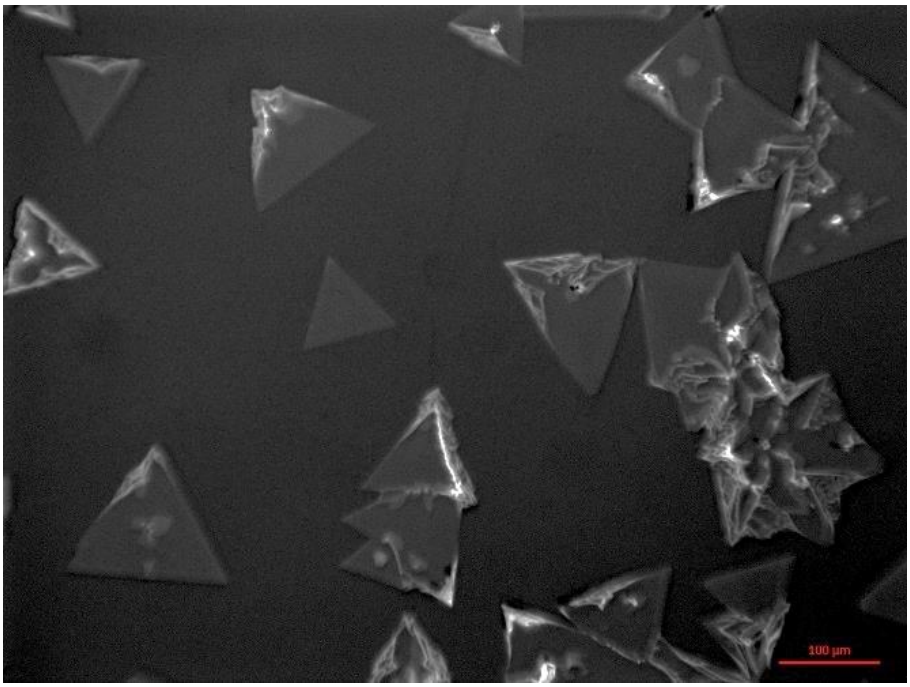

Figure 31: Optical microscope image of CVD grown pristine WS_2 triangles on Si/SiO_2. The image shown is representative of the sample and shows monolayer to few layer WS_2 triangles. The picture has been brightened for clarity, and the scale bar in the bottom right corresponds to 100 microns.

Figure 32 is a Raman spectrum of this pristine WS_2 sample taken at a laser excitation of 532 nm. The features on the spectrum are labeled in accordance with those documented in literature; those labeled in black correspond to monolayer WS_2 and those labeled in blue correspond to the SiO_2/Si substrate. The spectrum is representative of spectra taken at many other spots on the same sample. Comparing the spectrum to those shown in literature, it is clear that it corresponds to monolayer WS_2. Effort was taken to carry out subsequent SERS experiments on WS_2 monolayer regions. More analysis of Figure 32 is provided in the following section, "Analysis of Data."

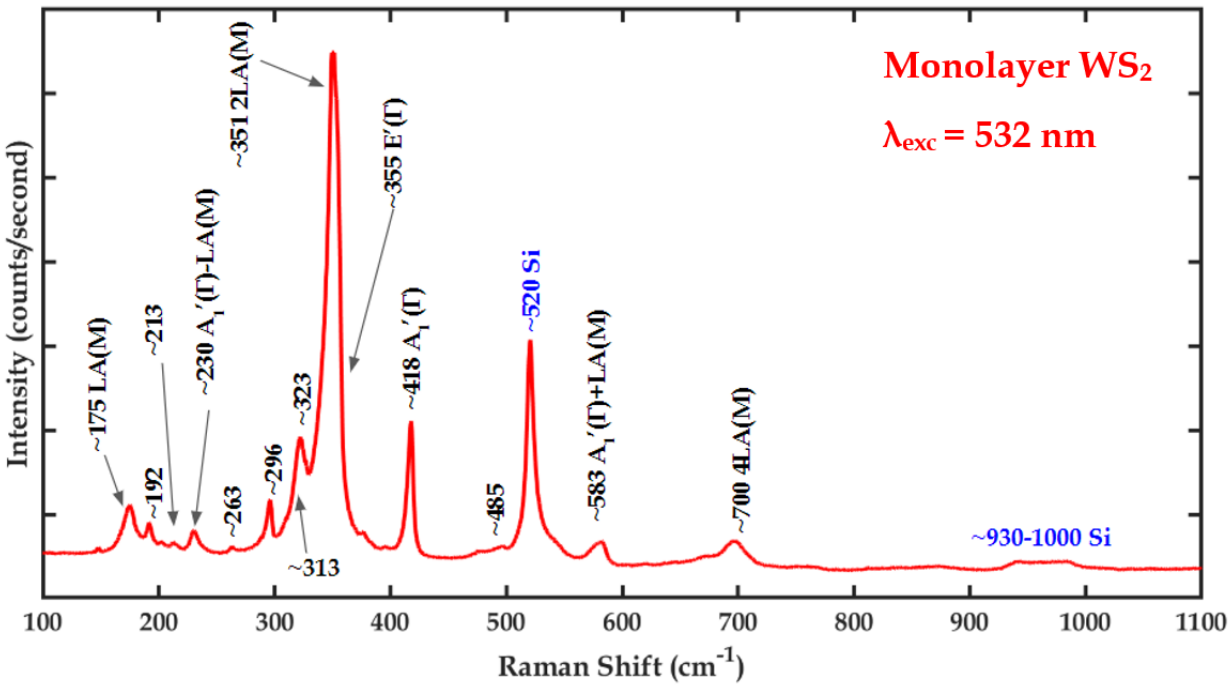

Figure 32: Raman spectrum of pristine WS_2 at laser excitation of 532 nm. The peaks labeled in black correspond to spectral features that are identified as characteristic of WS_2 monolayers in literature while those labeled in blue are characteristic of the SiO_2/Si substrate.

Figure 33 is a representative Raman spectrum of pristine graphene, grown by method 1, on SiO_2/Si. The laser excitation wavelength used was 488 nm. The spectral features labeled are

in accordance with literature, with the black labels corresponding to graphene features and the blue labels corresponding to the SiO_2/Si substrate.

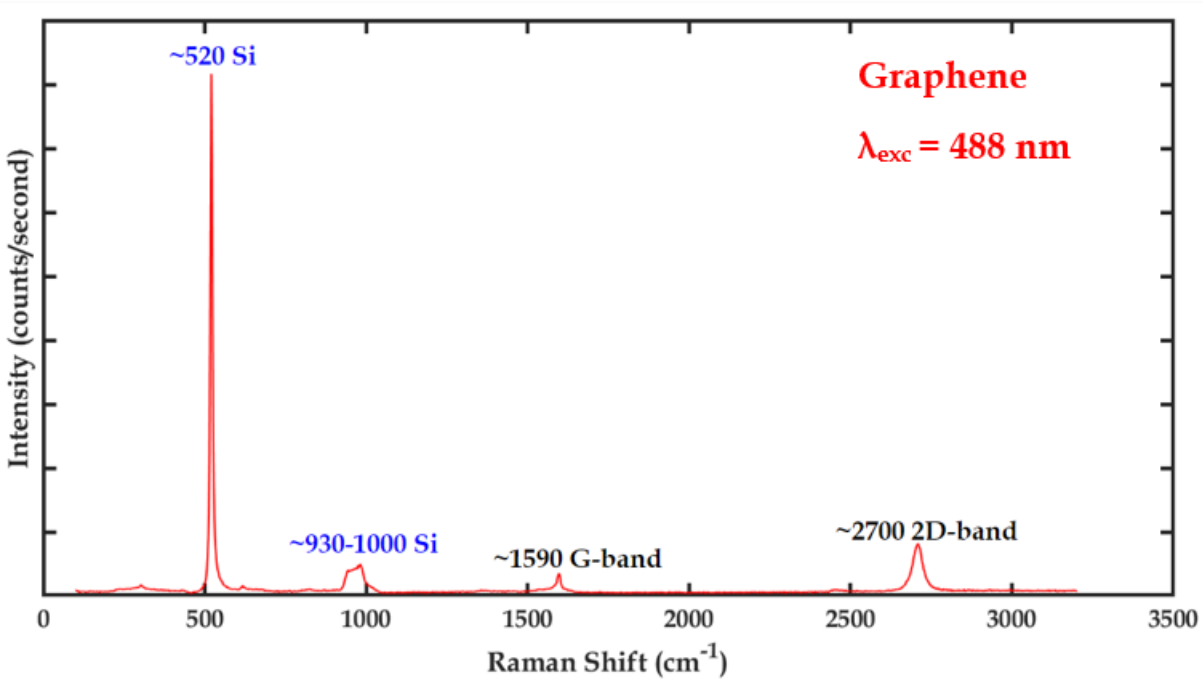

Figure 33: Raman spectrum of pristine graphene grown by method 1, taken at a 488 nm excitation. Graphene vibrational modes are labeled in black, while those corresponding to the SiO_2/Si substrate are labeled in blue.

Figure 34 is a representative Raman spectrum of pristine graphene grown by method 1; the spectrum is focused on the 1200 cm^{-1} to 3200 cm^{-1} range so that graphene spectral features can be resolved more clearly.

The graphene grown by method 2 varied more in uniformity, with many regions being multilayered. Figure 35 is a Raman spectrum from a multilayered region of a method 2 graphene sample; the excitation wavelength used was 532 nm.

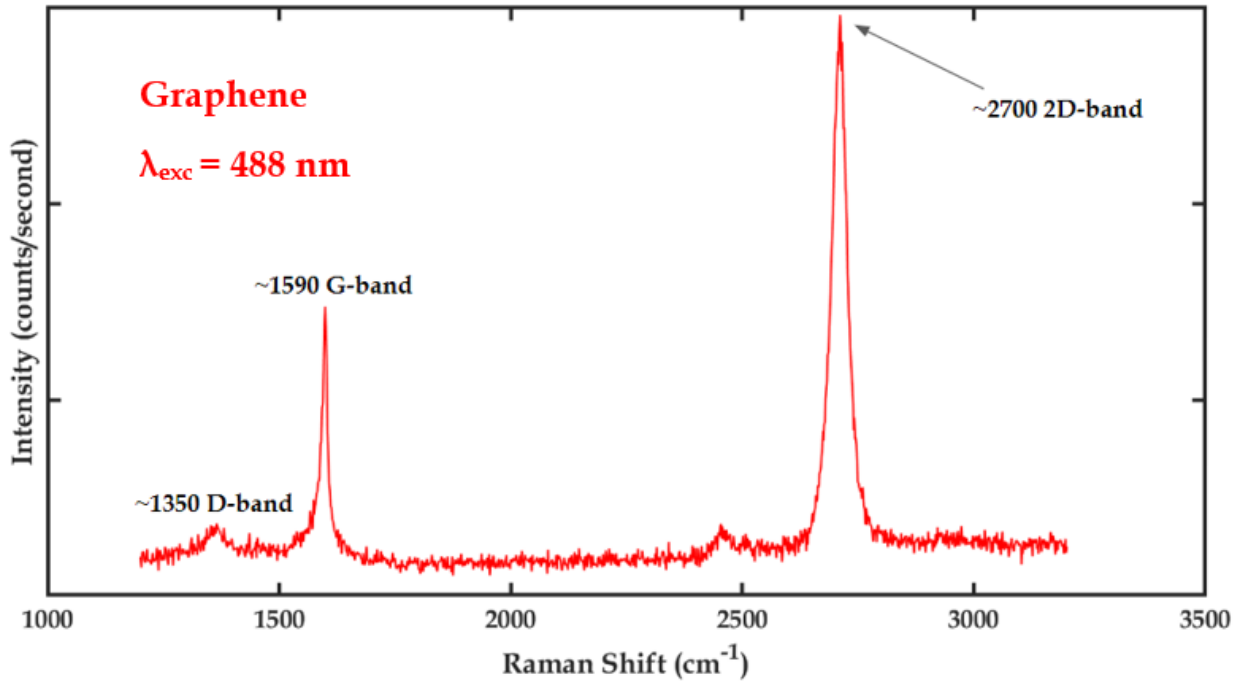

Figure 34: Representative Raman spectrum of graphene grown by method 1, taken at a 488 nm excitation: the spectrum is focused on the region where characteristic graphene vibrational modes, the D-, G-. and 2D- bands, are observed.

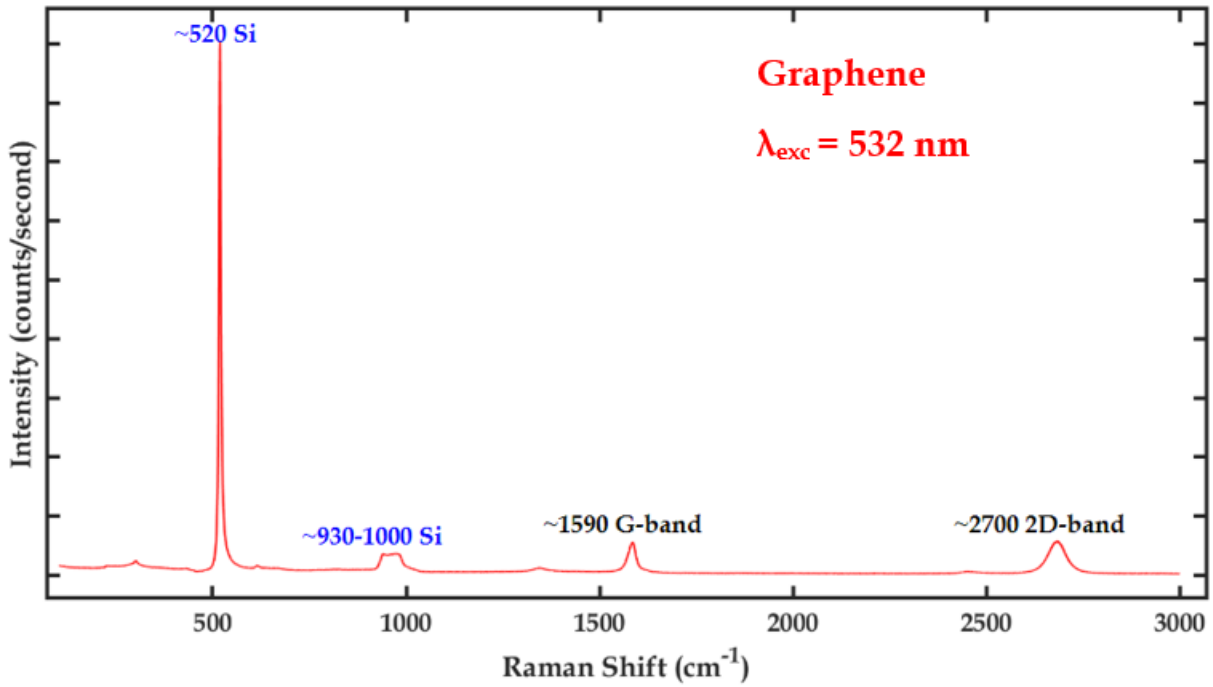

Figure 35: Raman spectrum of multilayered region of method 2 graphene at a 532 nm laser excitation: black labels are for graphene and blue labels are for SiO_2/Si modes.

Crystal Violet

10^{-5} M crystal violet was adsorbed on SiO_2/Si and the 2D material samples, graphene and monolayer WS_2, and Raman measurements were taken. On the bare silicon substrate (SiO_2/Si), fluorescence background was observed at 633 nm excitation, as seen in Figure 36

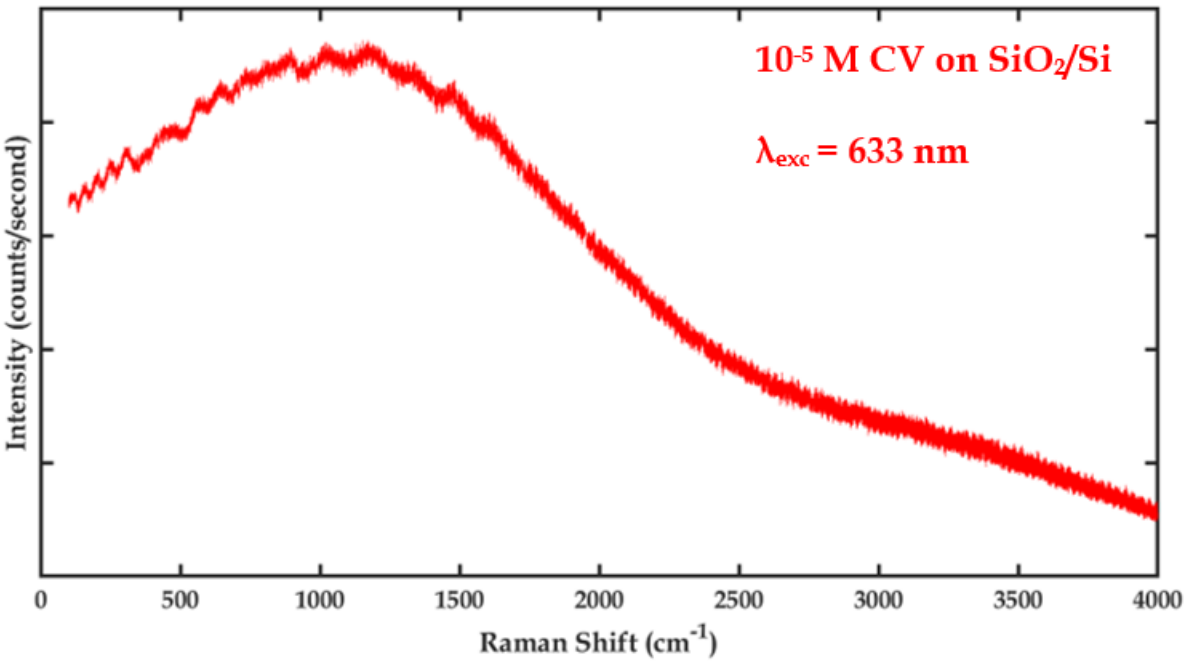

Figure 36: Fluorescence of CV on SiO_2/Si substrate at 633 nm excitation.

Figure 37 shows a Raman spectrum of crystal violet adsorbed on graphene, grown by method 1, and Figure 38 is a spectrum of crystal violet on graphene, grown by method 2. For both spectra, laser excitations of 532 nm were used. The black labels correspond to graphene Raman features while the violet labels correspond to crystal violet features noted in literature [68]. The blue labels are for the silicon substrate. Some crystal violet features, such as those at 1365 cm^{-1}, 1390 cm^{-1}, and 1620 cm^{-1} are closely positioned to graphene features, and so

it is difficult to distinguish whether they are crystal violet, graphene, or combination Raman modes. More analysis on these peaks is provided in later sections.

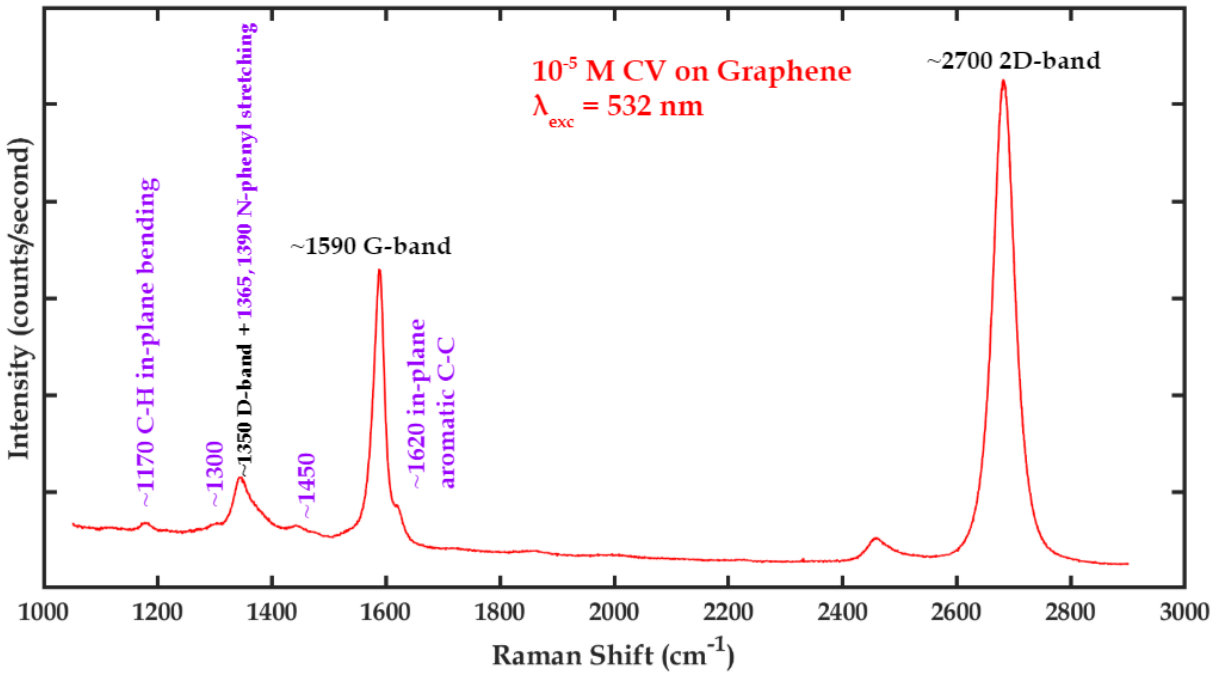

Figure 37: Raman spectrum of 10^{-5} M CV adsorbed on method 1 graphene at 532 nm excitation.

The ability of graphene samples to enhance crystal violet peaks, however, was inconsistent, as evidenced by Figure 39, which is a spectrum of CV adsorbed on a seemingly monolayer region of pristine graphene at an excitation of 532 nm. Interestingly, the 633 nm excitation which was thought to be resonant with the HOMO-LUMO gap of crystal violet from the literature referenced to construct Figure 30 did not distinguish CV peaks on graphene for any graphene sample.

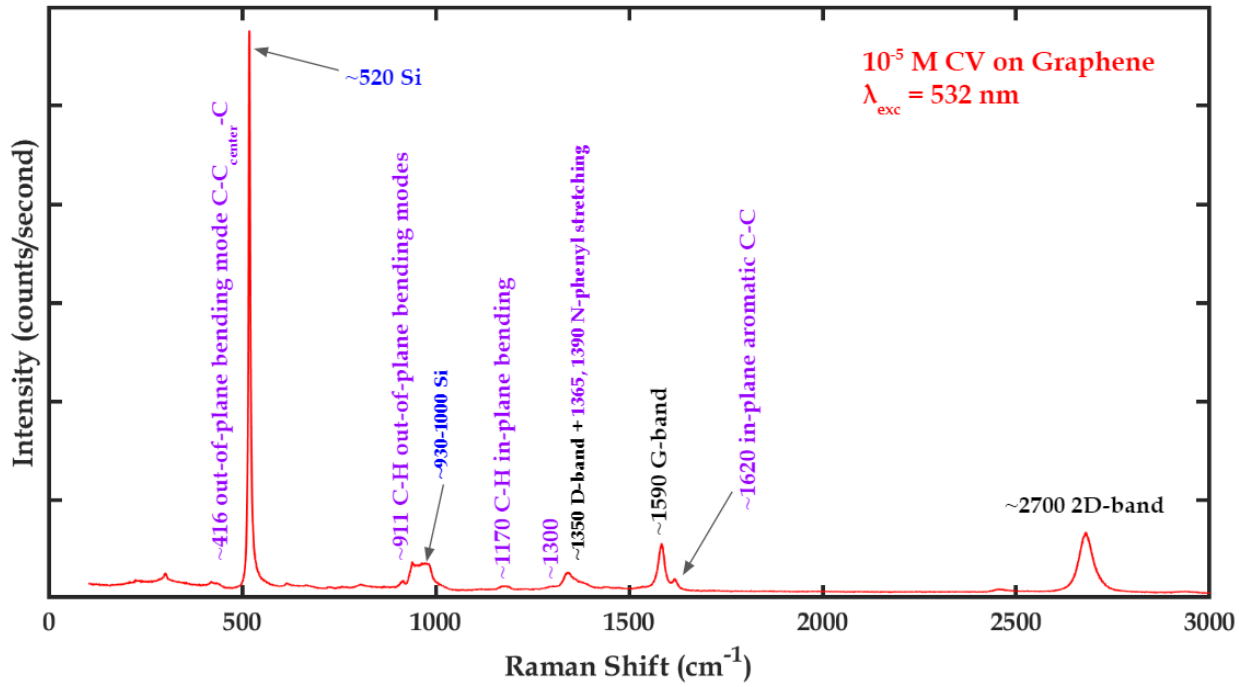

Figure 38: Raman spectrum of 10^{-5} M CV adsorbed on method 2 graphene at 532 nm excitation.

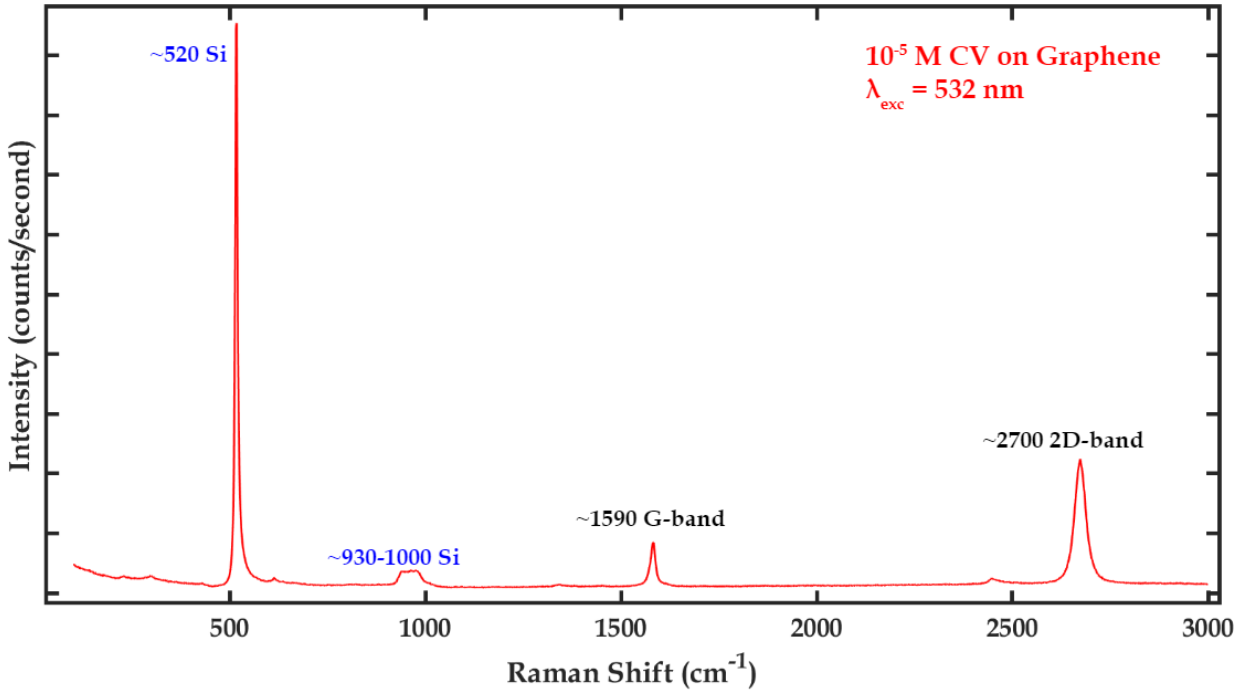

Figure 39: Raman spectrum of 10^{-5} M CV adsorbed on graphene in which no CV modes were observed.

Figure 40 is a spectrum of 10^{-5} M CV adsorbed on monolayer WS_2, at a laser excitation of 633 nm. The spectral features of CV and WS_2 are hidden by the fluorescence background from CV.

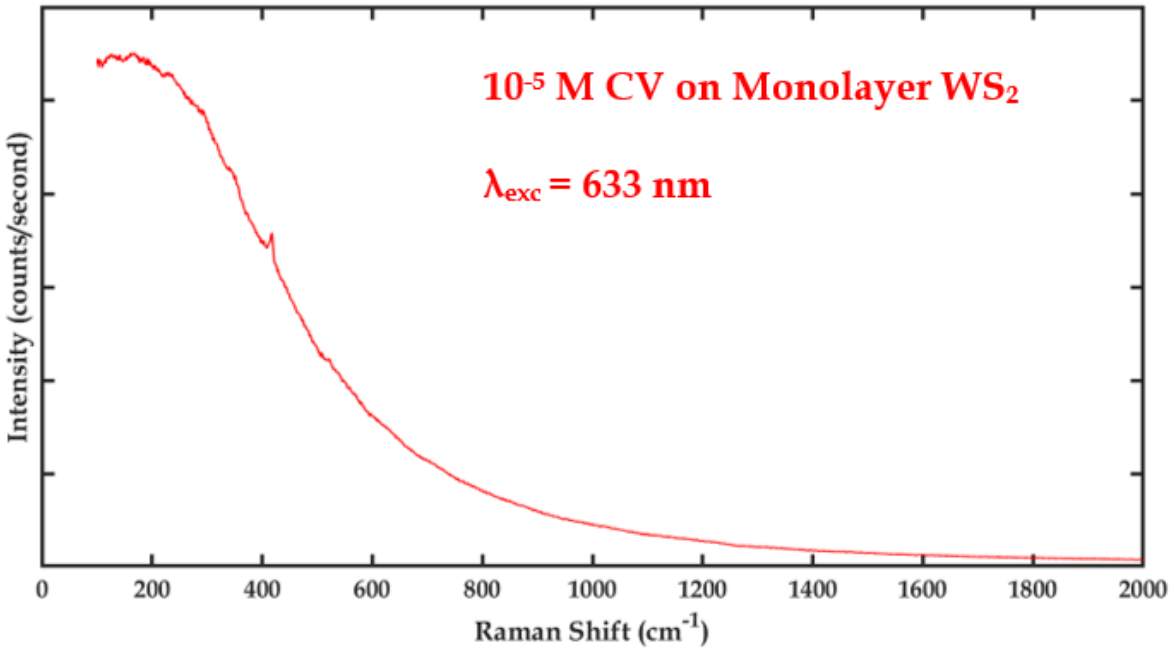

Figure 40: Fluorescence background from CV on WS_2 at 633 nm excitation.

At 532 nm excitations, fluorescence background was not observed, and WS_2 peaks were present in the spectrum; however, CV Raman features were not visible.

Rhodamine 6G

At a 532 nm excitation, the Raman spectrum of 10^{-5} M R6G adsorbed on SiO_2/Si was dominated by fluorescence background as shown in Figure 41.

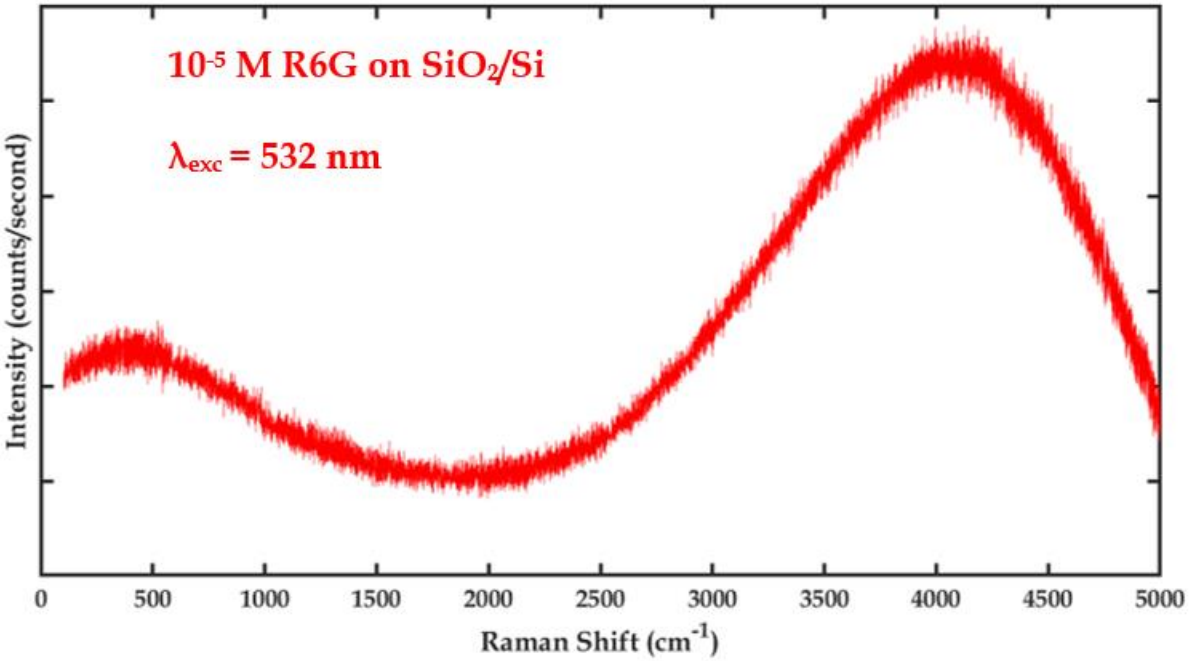

Figure 41: Fluorescence background from R6G on SiO_2/Si at 532 nm excitation.

As shown in Figure 42, fluorescence background was also present in Raman spectra of R6G on graphene, taken at an excitation of 532 nm. Figure 43 shows the same spectra in Figure 42 with the fluorescence background subtracted. The subtraction allows us to discern some R6G modes, which are labelled in orange in the figure.

Many R6G Raman modes were visible in the spectrum taken of R6G adsorbed on WS_2; this spectra, taken with a 532 nm laser excitation, is presented in Figure 44 with black labels for significant WS_2 modes, blue labels for features corresponding to the silicon substrate, and orange labels corresponding to R6G features identified in literature. The inset magnifies the portion of

the spectra that is particularly rich in R6G Raman modes. Table 2 gives the assignments of the R6G Raman modes based on literature [69], visible in Figure 44.

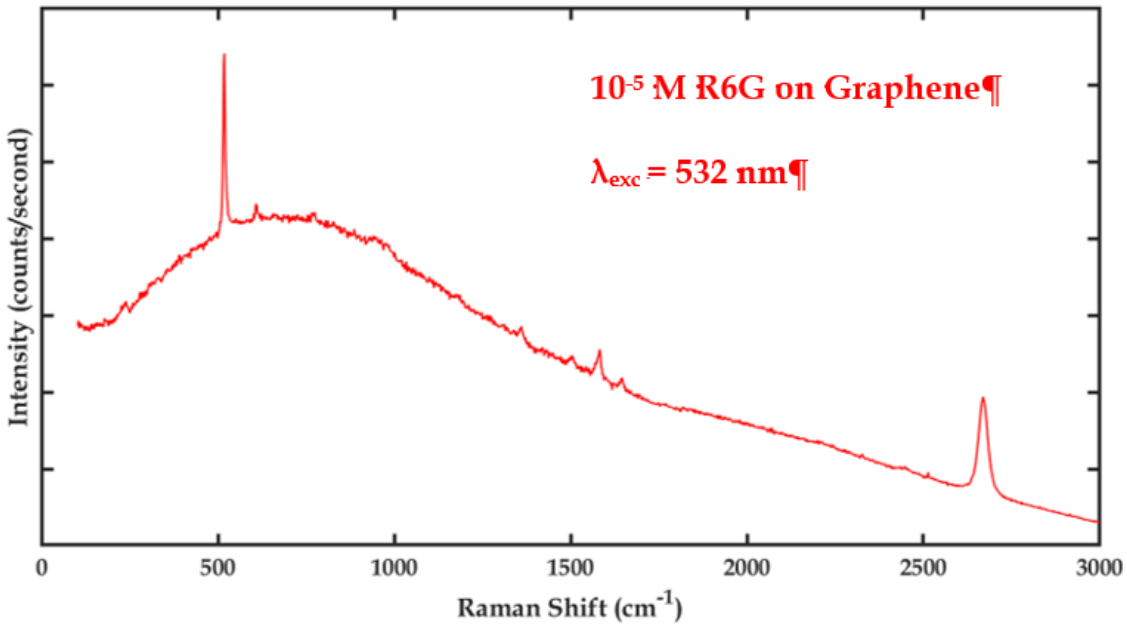

Figure 42: Raman spectrum of 10^{-5} M R6G on graphene at 532 nm excitation with fluorescence background.

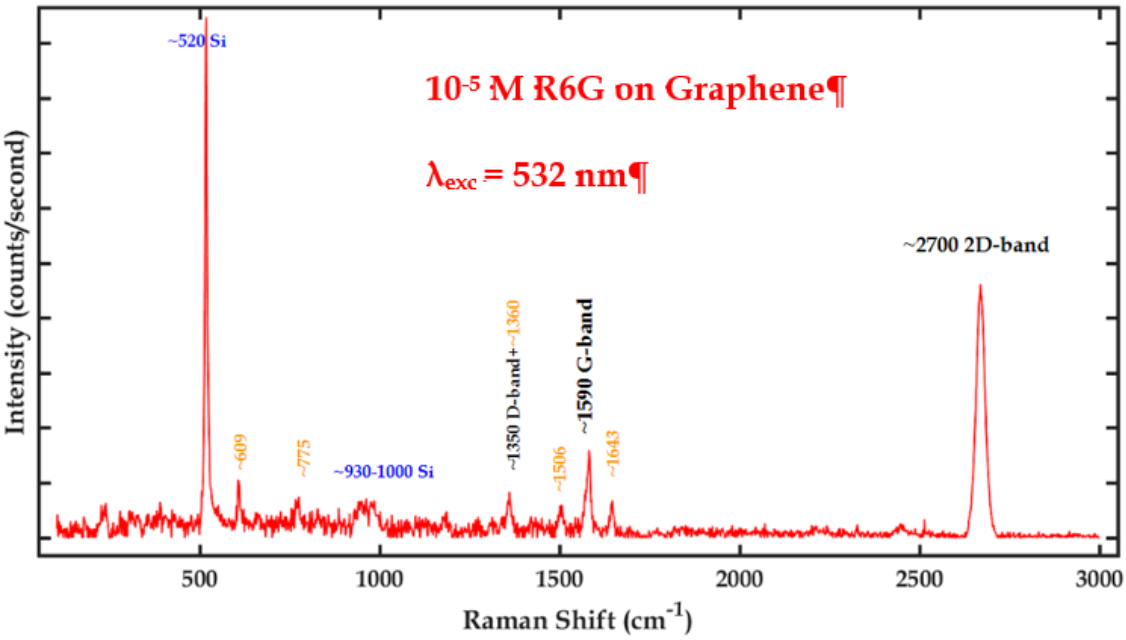

Figure 43: The same spectrum as Figure 42, but with fluorescence background subtracted.

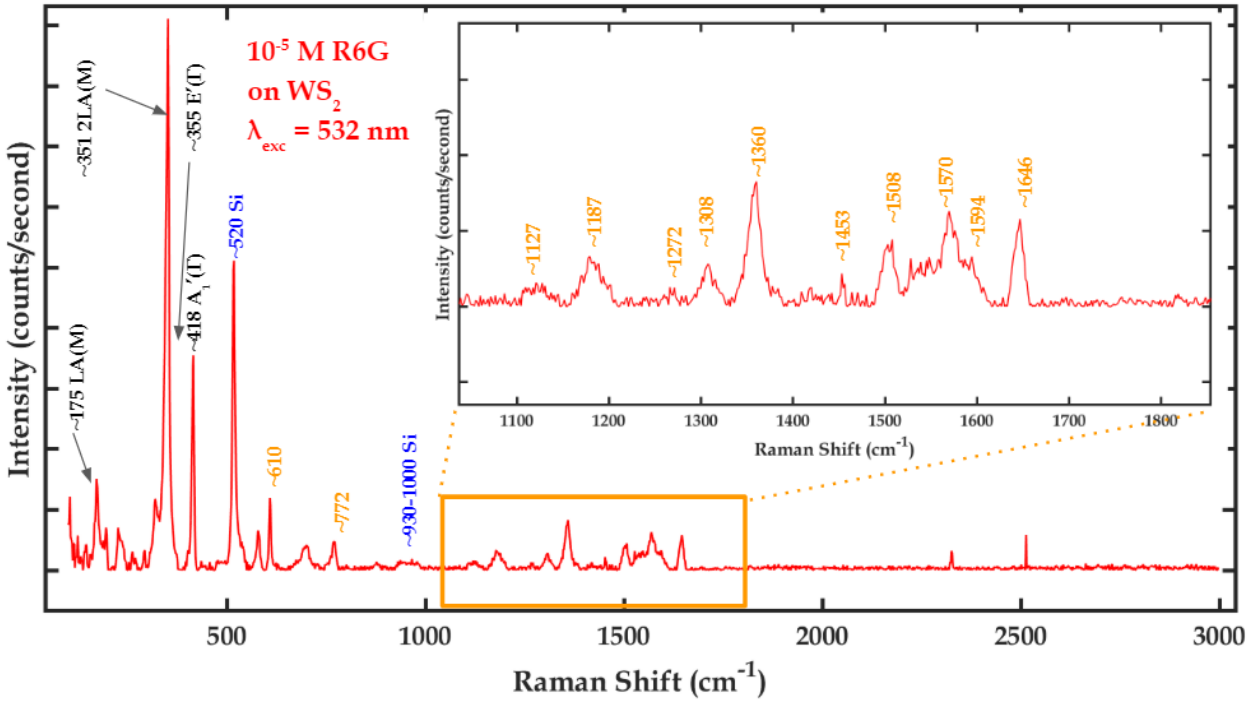

Figure 44: Raman spectrum of R6G adsorbed on WS_2 at 532 nm excitation; the modes labeled in orange are described in Table 2.

Table 2: Assignment of observed R6G peaks based on literature [69].

Raman mode (cm^{-1})	**Assignment**
610	C−C ring in-plane bending in xanthene/phenyl rings
772	C−H out-of-plane bending
1127	C−H in-plane bending in xanthene/phenyl rings
1187	C−H in-plane bending in xanthene ring
1272	C−O−C stretching in $COOC_2H_5$ group on phenyl ring
1308	hybrid mode (xanthene/phenyl rings and NHC_2H_5 group)
1360	C−C stretching in xanthene ring
1453	C−N stretching in NHC_2H_5
1508	C−C stretching in xanthene ring

1570	C−C stretching in phenyl ring
1594	hybrid mode (phenyl ring with $COOC_2H_5$)
1646	C−C stretching in xanthene ring

Rhodamine B

The Raman spectrum of 10^{-5} M RhB adsorbed on SiO_2/Si, at a 532 nm laser excitation, is shown in Figure 45 and dominated by RhB fluorescence background.

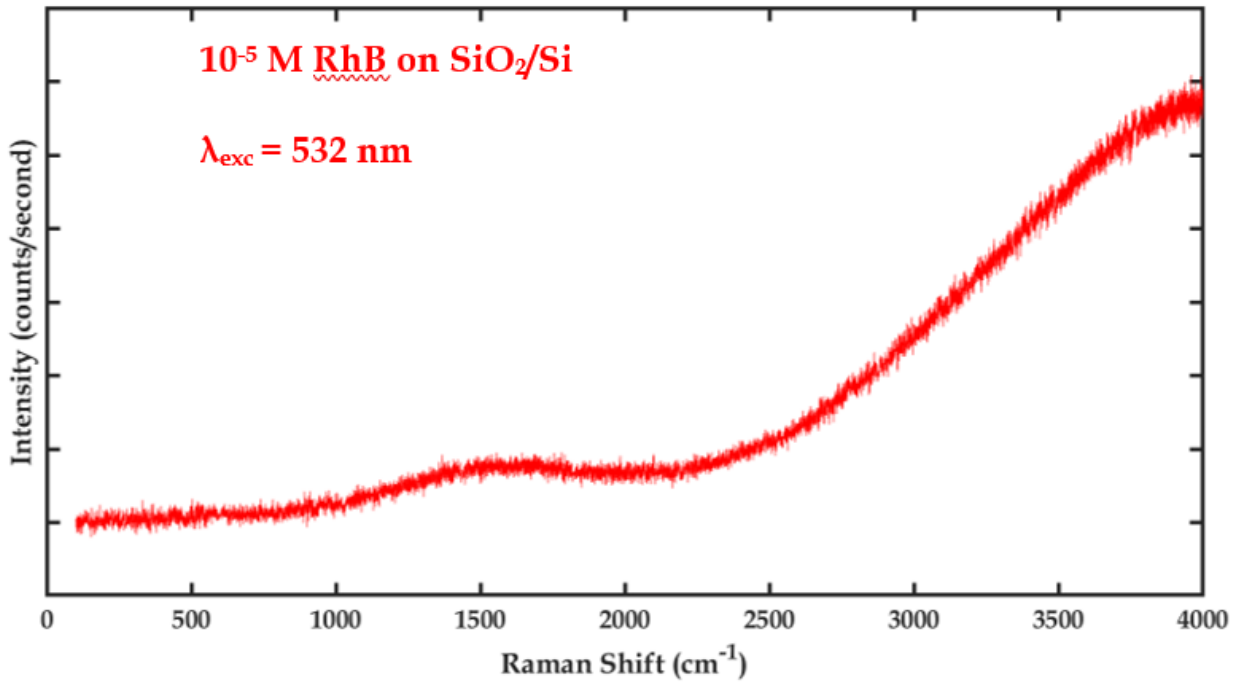

Figure 45: Fluorescence background from RhB on SiO_2/Si at a 532 nm excitation.

Fluorescence background from RhB was also observed in some cases on graphene. Figure 46 is a Raman spectrum of RhB on graphene, where fluorescence background is present.

Characteristic RhB Raman modes, which were also observed only occasionally on graphene, are labeled in pink in the figure.

Conversely, many RhB Raman modes were visible in the spectrum taken of RhB adsorbed on WS_2. A spectrum, taken with a 532 nm laser excitation, is presented in Figure 47 with black labels for significant WS_2 modes, the blue label for the silicon peak, and pink labels corresponding to RhB features identified in literature. The inset magnifies the portion of the spectra that is particularly rich in RhB Raman modes. Table 3 gives the assignments of the RhB Raman modes based on literature [70,71], visible in Figure 47.

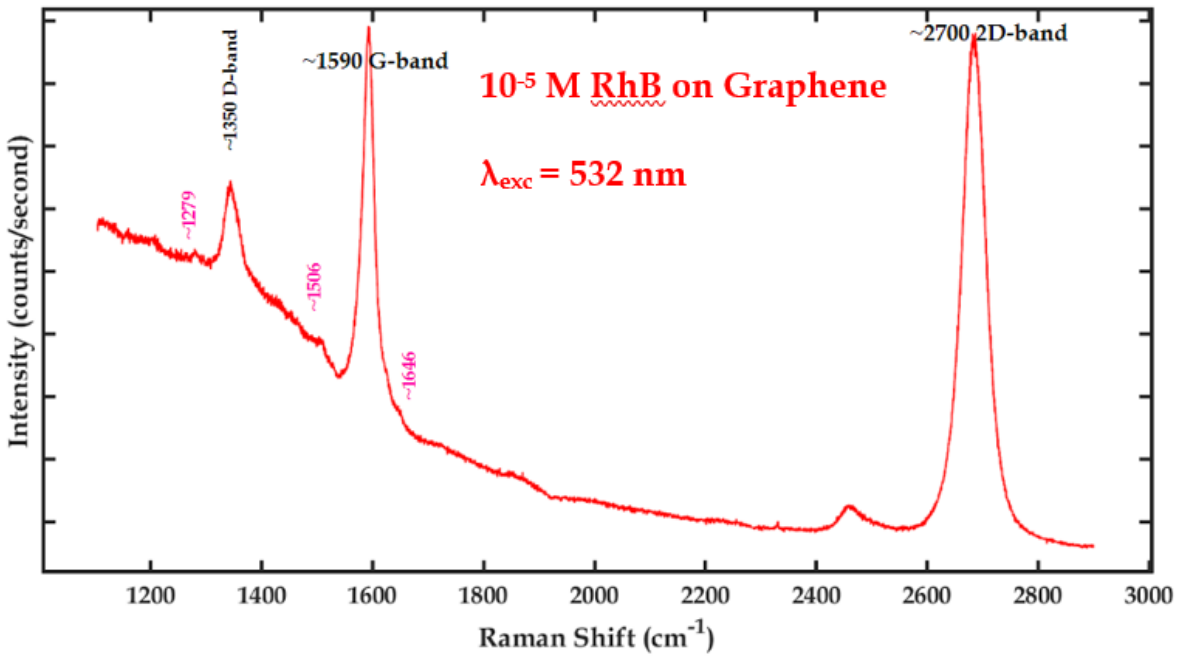

Figure 46: Raman spectrum of 10^{-5} M RhB on graphene at 532 nm excitation; a few RhB vibrational modes are observed though fluorescence background is present.

Conversely, many RhB Raman modes were visible in the spectrum taken of RhB adsorbed on WS_2. A spectrum, taken with a 532 nm laser excitation, is presented in Figure 47 with black labels for significant WS_2 modes, the blue label for the silicon peak, and pink labels corresponding to RhB features identified in literature. The inset magnifies the portion of the

spectra that is particularly rich in RhB Raman modes. Table 3 gives the assignments of the RhB Raman modes based on literature [70,71], visible in Figure 47.

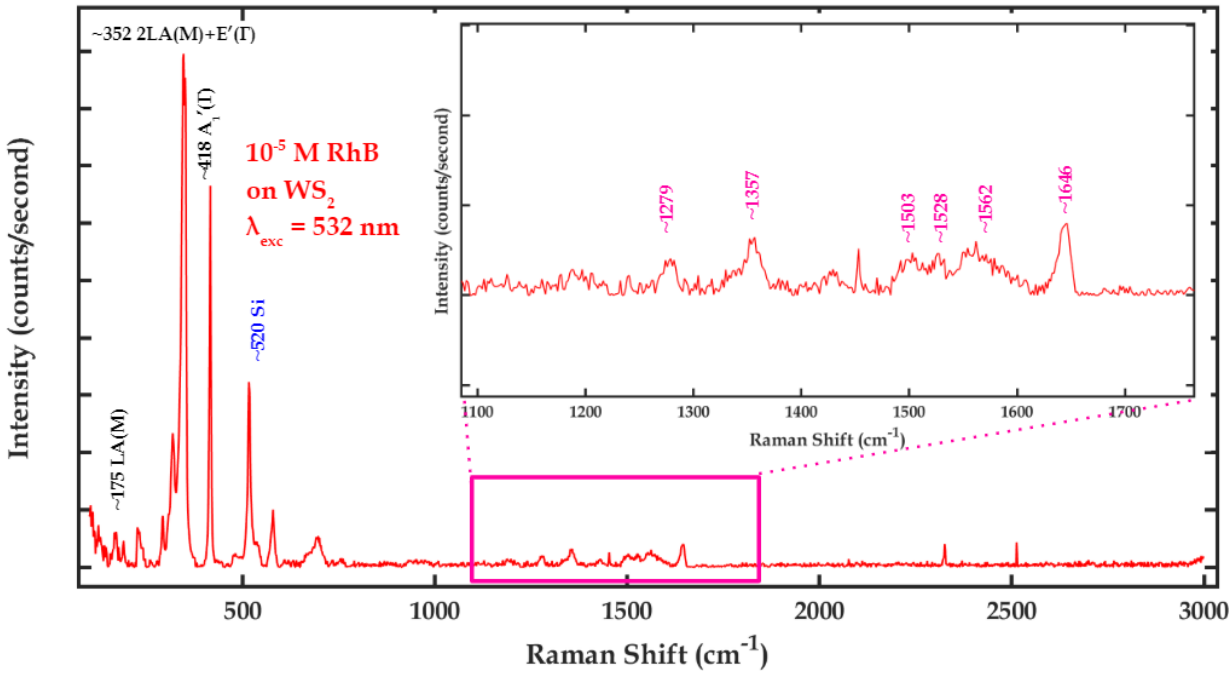

Figure 47: Raman spectrum of 10^{-5} M RhB on WS_2 at a 532 nm excitation; RhB vibrational modes are labeled in pink and described in Table 3.

Table 3: Assignment of observed RhB vibrational modes based on literature [70,71].

Raman mode (cm^{-1})	**Assignment**
1279	C−C ring in-plane bending in xanthene/phenyl rings
1357	C−H out-of-plane bending
1503	C−H in-plane bending in xanthene/phenyl rings
1528	C−H in-plane bending in xanthene ring
1562	C−O−C stretching in $COOC_2H_5$ group on phenyl ring
1646	hybrid mode (xanthene/phenyl rings and NHC_2H_5 group)

Analysis of Data

Baseline subtraction of noise was performed with an open source MATLAB function [67], which made use of a Savitzy-Golay filtering. To aid comprehension and to follow the conventions of literature, most of the spectra in the previous section are presented after filtering for noise. Spectra in Figure 36, Figure 40, Figure 41, Figure 42, Figure 45, and Figure 46 are presented in unprocessed form to point out the fluorescence background of the dyes. Graphene samples were not sufficiently uniform to allow for quantitative comparison. Hence, graphene's Raman features will be discussed more qualitatively, rather than quantitatively, in future sections.

The Raman spectra taken on WS_2 substrates were more comparable because the samples were taken from the same APCVD growth and there were sufficiently viable data obtained at the same laser excitation, 532 nm, for analysis. A quantitative comparison of the relative intensities of WS_2 Raman features between Figure 32, Figure 44, and Figure 47, which are spectra of WS_2, 10^{-5} M R6G adsorbed on WS_2, and 10^{-5} M RhB adsorbed on WS_2, respectively, is presented in Table 4.

Table 4: Relative intensities of WS_2 Raman modes at 532 nm excitations for three different Raman spectrum: the spectrum of WS_2 in Figure 32, the spectrum of R6G on WS_2 in Figure 44, and the spectrum of RhB on WS_2 in Figure 47; the data presented in the table could be useful to assess the quality of the WS_2 substrate used for the R6G and RhB measurements.

Spectra	$I_{2LA+E'}/I_{A_1'}$	$I_{LA}/I_{A_1'}$	A_1' position (cm^{-1})
Raman of WS_2 (Figure 32)	3.08	0.527	418
Raman of 10^{-5} M R6G on WS_2 (Figure 44)	2.57	0.425	416
Raman of 10^{-5} M RhB on WS_2 (Figure 47)	1.35	0.0926	416

The Raman features of the dyes are discussed qualitatively as part of the interpretation of the enhancing ability of the substrates in the following sections.

Chapter 6

Discussion

Interpretation of Data

2D Material Samples

The spectrum shown in Figure 32 is that of a pristine monolayer WS_2 triangle. The spectrum is taken at a spot away from the edge of the triangular island and with a laser excitation wavelength of 532 nm. Although previous literature points to the 2LA(M) mode being resonant at 514.5 nm excitations, the 532 nm excitation seems close enough in energy to excite this strong resonance, which is evidenced by the fact that the 2LA(M) mode is considerably larger in intensity than is the A_1'(Γ) mode. This strong resonance of the 2LA(M) mode, which overlaps with the E'(Γ) mode, is a facile confirmation that this particular triangle is a monolayer region. The shoulder at ~485 cm^{-1} is a commonly seen feature for WS_2 synthesized by atmospheric pressure chemical vapor deposition, which was the method of synthesis for WS_2 samples in this study. The intensity of the LA(M) mode has been correlated with the inverse of the average interdefect length squared, and so its prominence in the spectrum in Figure 32 indicates the presence of defects, which could include sulfur vacancies, WS_x vacancies, and grain boundaries.

Figure 33, Figure 34, and Figure 35 are Raman spectra of graphene samples. The variation in the ratio of the intensities of the 2D to G peaks in the spectra indicates that the thickness of the samples was not uniform; this was particularly evident in the samples grown by method 2 and was corroborated by inspecting these samples with an optical microscope, as they

appeared to have monolayer, bilayer, and few layer regions. Also, the prevalence of a small D peak in the spectra shown in Figure 34 indicates the presence of disorder, likely due to defects.

Crystal Violet

The ability of graphene to probe the Raman features of 10^{-5} M CV was inconsistent. At some spots on graphene samples, CV Raman features could be discerned, as in Figure 37 and Figure 38. As seen in Figure 39, however, at other spots, graphene did not enhance any CV Raman modes. Figure 39 appears to be a spectrum taken at a fairly pristine monolayer region—as the D-band is barely visible, and the ratio of the 2D to G peak is approximately two. Interestingly, the spectra in Figure 37 and Figure 38 have more prominent D-bands when compared to the spectrum in Figure 39; perhaps, this could suggest that more defective spots showed better Raman enhancing capability for CV. However, the data of CV on graphene were too inconsistent to confirm such a trend outright.

Even in the spectra that show CV Raman modes on graphene substrates (Figure 37 and Figure 38), many characteristic CV Raman features thar are identified in literature are missing. These missing Raman features include an out-of-plane aromatic C-C formation (~555 cm^{-1}) and a C-N-C symmetric stretching vibration (~720 cm^{-1}). Also, a bending mode of C-N-C and in-plane aromatic C-C have been observed at Raman shifts of ~520 cm^{-1} and ~1582 cm^{-1}, respectively; these modes overlap with the Si/SiO_2 peak and the G-band of graphene, respectively, and this may explain why they are not visible in the spectra shown in Figure 37 and Figure 38. Furthermore, the D-band in graphene at ~1350 cm^{-1} in Figure 37 and Figure 38 appears prolonged in its descent to the right of the peak, indicating the presence of characteristic

CV modes, namely stretching vibrations of the nitrogen and phenyl rings in CV at ~1365 cm^{-1} and ~1390 cm^{-1}. Nevertheless, many of the characteristic CV Raman modes previously assigned in literature are close in proximity to the characteristic spectral features of the graphene and silicon substrates used, and so pristine graphene may not be as ideal a Raman-enhancing substrate for CV as an analysis of energy-level alignment might suggest. Moreover, the CV features that were detected on the graphene substrate, appeared to be rather weak in intensity relative those of CV on nitrogen doped graphene reported by Feng et al.

However, on WS, no CV Raman modes were observed at 532 nm or 633 nm excitations, and so, as was predicted by our analysis of energy-level alignment, graphene was a more effective Raman-enhancing substrate for CV than WS_2.

Fluorescence of CV was observed at 633 nm excitations on SiO_2/Si and WS_2, which suggests that this excitation approximately corresponds to the transition between electronic states—namely that between the HOMO and LUMO in CV. Furthermore, this suggests that the 633 nm excitation would be ideal for resonance Raman enhancement and should provide the best Raman enhancement for CV adsorbed on graphene. However, we found the 633 nm excitation to be ineffective for probing CV modes on graphene; the 532 nm laser was the excitation at which we were most successful at probing CV modes. Perhaps, this could be understood from the analysis of Feng et al., who note that CV, a cation, could interact electrostatically with graphene's electronic density through the induction of image charges, and the electric field of these image charges can shift the positions of energy levels. In fact, Feng et al. report the HOMO-LUMO gap of CV on pristine graphene to be 2.62 eV. Though we have defects in our samples, meaning most of our graphene samples are not quite pristine, the 532 nm excitation is likely closer to the HOMO-LUMO gap of CV on graphene than is the 633 nm excitation.

Rhodamine 6G

The Raman modes of 10^{-5} M R6G on WS_2 were well enhanced, as shown in Figure 44. Of the prominent modes previously assigned and identified in literature, the only two that are not clearly identified in the spectra in Figure 44 are a hybrid mode at 797 cm^{-1}, corresponding to xanthene/phenyl rings and the NHC_2H_5 group, and a hybrid mode at 1204 cm^{-1}, corresponding to xanthene/phenyl rings. The other prominent modes are clearly enhanced and present in Figure 44 and described in Table 2. Interestingly, the R6G modes most strongly enhanced when adsorbed on WS_2 are bending and stretching vibrations associated with C-C bonds in R6G. Examining the WS_2 features in the spectra indicates that it is likely taken at a monolayer region (given the resonance of the 2LA(M) + E'(Γ) combination mode and the intensity of this mode compared to that of A_1'(Γ)) with considerable defect density (given the prominence of the LA(M) mode which has been correlated to defects).

As predicted, graphene was less successful in probing R6G modes. However, as shown in Figure 43, a few R6G modes were weakly enhanced on graphene. It is also interesting that there is considerable fluorescence background in Figure 42 at a 532 nm excitation on graphene—though not as much fluorescence as was observed on the bare SiO_2/Si substrate. WS_2 substrates were more effective in quenching R6G fluorescence as very little baseline subtraction was employed to obtain the spectrum in Figure 44.

Rhodamine B

Raman modes from 10^{-5} RhB adsorbed on graphene were barely visible. Only a few weak shoulders or peaks can be discerned from the spectra in Figure 46. What appeared to be

fluorescence background was present in some spectra taken of RhB on graphene, but not always. There is no evident explanation for why this fluorescence was observed only occasionally. Characteristic RhB Raman modes were observed on graphene only occasionally and the intensities of these modes were very weak.

WS_2 appears to be a more effective Raman-enhancing substrate for RhB than graphene, which corroborates our hypothesis founded on the proximity of energy levels in the adsorbate and the substrate. Six of the RhB Raman modes previously reported in literature are enhanced in the spectrum in Figure 47; there is not an apparent connection between the types of RhB modes enhanced on WS_2. Many other characteristic RhB Raman modes previously identified in literature, including a couple of aromatic bending modes at ~620 cm^{-1} and ~1200 cm^{-1}, are missing from the spectrum. Fluorescence background from RhB was mostly quenched by the WS_2 substrate and very little baseline subtraction was employed to produce the spectrum seen in Figure 47.

Given that theoretical value for the Fermi energy of WS_2 reported in Figure 30 is about midway between the theoretical values for the LUMOs of RhB and R6G, it was expected that the success of the WS_2 substrate in enhancing the Raman modes of RhB and R6G would be relatively similar. Unexpectedly, twice as many R6G modes than RhB modes were probed on WS_2. However, this is probably more due to the difference in the WS_2 substrate used for each dye rather than any notable interaction between each dye and WS_2 or any properties of the dyes. The CVD grown WS_2 used in these experiments were cut into four pieces: one for pristine Raman measurements, one for CV measurements, one for RhB measurements, and one for R6G measurements. Table 4 allows us to compare the WS_2 substrates used for Raman measurements on R6G and RhB. It is apparent that the ratio of the intensity of the combination 2LA(M) + E’(Γ)

mode to the intensity of the A_1'(Γ) mode is higher in Figure 44 than in Figure 47. Also, the relative intensity of the LA(M) mode, in comparison to the intensity of the A_1' mode, in Figure 44 is higher than that in Figure 47. This suggests that there was some variation in the WS_2 substrates used for R6G and RhB experiments: the spectra indicate that the WS_2 piece used for R6G experiments showed more characteristics of a monolayer and greater defect density. Previous research indicates that defects in substrates can act as reaction centers that change the interaction of an organic adsorbate and inorganic substrate and aid in charge transfer [72]. It is noteworthy that the substrates that were successful in enhancing Raman modes of dyes in this study showed some evidence of defects in their Raman features.

Impact

The spectra obtained of the dyes adsorbed on WS_2 seem to follow our predictions based on energy-level alignment—that WS_2 is successful at enhancing Raman modes on R6G and RhB, but not on CV. The proximity of the Fermi level of WS_2 to the LUMO of the dye appears, in this study, to correlate with Raman enhancement. Graphene samples were not uniform, and so it is difficult to make outright conclusions from the spectra taken on graphene; still, graphene served as a useful comparison to our WS_2 substrates. In general, there appears to be a trend that correlates defects in 2D material substrates to their Raman-enhancing capability. All of the spectra which enhanced Raman modes of the dyes showed some evidence for the presence of defects. Furthermore, the substrates with supposedly high defect density, such as the piece of WS_2 that R6G was adsorbed on, fared the best in probing Raman modes of the dyes. As explored in previous research, it is quite possible that defects in the substrates aided in charge transfer

between the substrate and the adsorbate. Also, it has been proposed that defects serve to quench fluorescence in dyes as they act as trap sites that prevent electron-hole recombination. Overall, these results offer support to the notion that the Raman-enhancing mechanism in WS_2 is similar to the charge transfer mechanism previously explored on graphene and doped graphene in GERS. The results of this study justify further work to rigorously elucidate the Raman-enhancing mechanism in WS_2 and other 2D materials.

Chapter 7

Summary and Conclusions

Graphene and WS_2 films were synthesized via APCVD. Graphene was transferred from the Cu foil it was grown on to a SiO_2/Si (silicon) substrate while WS_2 was synthesized directly on the silicon substrate. Three chemical dyes, 10^{-5} M CV, 10^{-5} M R6G, and 10^{-5} M RhB were prepared and adsorbed on graphene and WS_2. The Raman spectra of the dyes on the 2D material substrates were collected. Based on previous theoretical and experimental research, we formulated a hypothesis that the proximity of the LUMO of the adsorbed dye to the Fermi energy of the 2D material substrate would enhance the charge transfer between the substrate and the dye under a resonant excitation close in energy to the HOMO-LUMO gap of the dye. Thus, we predicted that the Raman modes of RhB, with its LUMO positioned at -2.73 eV with respect to the vacuum energy, and R6G, with its LUMO positioned at -3.40 eV with respect to vacuum energy, would be better enhanced on WS_2 (Fermi energy at -3.00 eV relative to the vacuum level) substrates than on graphene (Fermi energy at -4.60 eV relative to vacuum level) substrates. By the same analysis, Raman modes of CV, with a LUMO positioned at -4.10 eV, were predicted to be better probed on graphene than WS_2.

The spectra collected in this study mostly followed these predictions. Many characteristic R6G modes (those at 610 cm^{-1}, 772 cm^{-1}, 1127 cm^{-1}, 1187 cm^{-1}, 1272 cm^{-1}, 1308 cm^{-1}, 1360 cm^{-1}, 1453 cm^{-1}, 1508 cm^{-1}, 1570 cm^{-1}, 1594 cm^{-1}, and 1646 cm^{-1}) were well-enhanced on WS_2 at 532 nm excitations. On graphene with a 532 nm excitation, some fluorescence background from R6G was observed, but after subtracting this background, some of the R6G modes (those at 610 cm^{-1}, 775 cm^{-1}, 1360 cm^{-1}, 1508 cm^{-1}, and 1646 cm^{-1}) were visible; the modes were weaker in intensity, relative to other spectral features, on graphene than on WS_2. RhB modes were also

better enhanced on WS_2 than on graphene. Graphene did not always quench the fluorescence background from RhB at 532 nm excitations, and only enabled us to see a few RhB modes (1279 cm^{-1}, 1506 cm^{-1}, and 1646 cm^{-1}) that were weak in intensity. On WS_2 at 532 nm excitations, more RhB vibrations were observed (1279 cm^{-1}, 1357 cm^{-1}, 1503 cm^{-1}, 1528 cm^{-1}, 1562 cm^{-1}, and 1646 cm^{-1}). No CV modes were observed on WS_2, and at 633 nm excitations, the spectra were dominated by significant fluorescence background. On graphene at 532 nm excitations, some weak CV modes were observed (416 cm^{-1}, 911 cm^{-1}, 1170 cm^{-1}, 1300 cm^{-1}, 1365 cm^{-1}, 1390 cm^{-1}, and 1620 cm^{-1}), but the results were inconsistent. The presence of defects in the 2D material substrates seemed to correlate with better Raman enhancement; it is supposed that defects aid in charge transfer and fluorescence quenching based on previous research.

In general, the results support the hypothesis outlined in the Methodology section, which is founded on the charge transfer Raman enhancement mechanisms proposed by Feng et al. in graphene and nitrogen doped graphene. Furthermore, these results suggest that the Raman enhancement mechanism in WS_2 substrates is similar. Continued study of the Raman enhancement of molecules on 2D material substrates is warranted.

The Engineering Science and Mechanics department protocols require a discussion of ethics, economics, and safety in this research. Laboratory protocols were followed and effort was taken to ensure safe and ethical research practices; however this research does not directly evaluate or study ethical or professional responsibility, or laboratory or research safety. Since the focus of this research was targeted at understanding a useful phenomenon observed in science, the economic issues associated with the work are not directly addressed.

Chapter 8

Future Work

Further work could be done to more rigorously study the Raman enhancing capabilities of 2D material substrates. It would be prudent to repeat some parts of this study with more uniform graphene samples and also to explore the detection limits of 2D materials surfaces beyond 10^{-5} M solutions. Similar to the work Feng et al. carried out with graphene and nitrogen doped graphene, it would be informative to dope WS_2 and other 2D materials, explore the effect that doping has on the energy level alignment adsorbed molecules, and characterize the Raman enhancement. Another approach to test the proposed enhancement mechanism could be to fabricate a device, such as a transistor, with a 2D material channel, vary gate biases to shift the Fermi level of the 2D material between Raman measurements, and study the effect of Fermi level positioning on the Raman enhancement of adsorbed molecules, similar to the work of Xu et al [73]. Numerous other 2D materials and molecules could be studied. Also, given the need for faster disease detection, particular emphasis could be given to exploring the ability of 2D materials to identify and detect biological molecules and viruses via enhanced Raman spectroscopy.

BIBLIOGRAPHY

[1] S. Feng, M. Cristina dos Santos, B. R. Carvalho, R. Lv, Q. Li, K. Fujisawa, A. L. Elías, Y. Lei, N. Perea-López, M. Endo, M. Pan, M. A. Pimenta, and M. Terrones, Sci. Adv. (2016).

[2] X. Ling, W. Fang, Y. H. Lee, P. T. Araujo, X. Zhang, J. F. Rodriguez-Nieva, Y. Lin, J. Zhang, J. Kong, and M. S. Dresselhaus, Nano Lett. (2014).

[3] K. S. Novoselov, A. K. Geim, S. V. Morozov, D. Jiang, Y. Zhang, S. V. Dubonos, I. V. Grigorieva, and A. A. Firsov, Science (80-.). (2004).

[4] D. Akinwande, N. Petrone, and J. Hone, Nat. Commun. **5**, 5678 (2014).

[5] M. Bernardi, M. Palummo, and J. C. Grossman, Nano Lett. **13**, 3664 (2013).

[6] J. Yoon, W. Park, G.-Y. Bae, Y. Kim, H. S. Jang, Y. Hyun, S. K. Lim, Y. H. Kahng, W.-K. Hong, B. H. Lee, and H. C. Ko, Small **9**, 3295 (2013).

[7] F. Bonaccorso, Z. Sun, T. Hasan, and A. C. Ferrari, Nat. Photonics **4**, 611 (2010).

[8] A. Gupta, T. Sakthivel, and S. Seal, Prog. Mater. Sci. **73**, 44 (2015).

[9] R. Lv, G. Chen, Q. Li, A. McCreary, A. Botello-Méndez, S. V. Morozov, L. Liang, X. Declerck, N. Perea-López, D. A. Cullen, S. Feng, A. L. Elías, R. Cruz-Silva, K. Fujisawa, M. Endo, F. Kang, J. C. Charlier, V. Meunier, M. Pan, A. R. Harutyunyan, K. S. Novoselov, and M. Terrones, Proc. Natl. Acad. Sci. U. S. A. (2015).

[10] A. Silver, H. Kitadai, H. Liu, T. Granzier-Nakajima, M. Terrones, X. Ling, and S. Huang, Nanomaterials (2019).

[11] Q. H. Wang, K. Kalantar-Zadeh, A. Kis, J. N. Coleman, and M. S. Strano, Nat.

Nanotechnol. **7**, 699 (2012).

[12] A. H. Castro Neto, F. Guinea, N. M. R. Peres, K. S. Novoselov, and A. K. Geim, Rev. Mod. Phys. **81**, 109 (2009).

[13] R. Lv, M. C. Dos Santos, C. Antonelli, S. Feng, K. Fujisawa, A. Berkdemir, A. L. Elías, N. Perea-Lopez, M. Terrones, R. Cruz-Silva, F. López-Urías, and H. Terrones, Adv. Mater. (2014).

[14] W. Zhang, L. Wu, Z. Li, and Y. Liu, RSC Adv. (2015).

[15] T. Granzier-Nakajima, K. Fujisawa, V. Anil, M. Terrones, and Y.-T. Yeh, Nanomaterials (2019).

[16] D. Wickramaratne, L. Weston, and C. G. Van de Walle, J. Phys. Chem. C **122**, 25524 (2018).

[17] W. Choi, I. Lahiri, R. Seelaboyina, and Y. S. Kang, Crit. Rev. Solid State Mater. Sci. (2010).

[18] M. S. A. Bhuyan, M. N. Uddin, M. M. Islam, F. A. Bipasha, and S. S. Hossain, Int. Nano Lett. **6**, 65 (2016).

[19] Q. Cai, S. Mateti, K. Watanabe, T. Taniguchi, S. Huang, Y. Chen, and L. H. Li, ACS Appl. Mater. Interfaces **8**, 15630 (2016).

[20] S. Nakhaie, J. M. Wofford, T. Schumann, U. Jahn, M. Ramsteiner, M. Hanke, J. M. J. Lopes, and H. Riechert, Appl. Phys. Lett. **106**, 213108 (2015).

[21] A. Govind Rajan, J. H. Warner, D. Blankschtein, and M. S. Strano, ACS Nano **10**, 4330 (2016).

[22] A. K. Geim and K. S. Novoselov, Nat. Mater. (2007).

[23] H. P. Boehm, A. Clauss, G. O. Fischer, and U. Hofmann, Zeitschrift Für Anorg. Und Allg.

Chemie **316**, 119 (1962).

[24] Z. Sun, D. K. James, and J. M. Tour, J. Phys. Chem. Lett. (2011).

[25] S. Agnoli and M. Favaro, J. Mater. Chem. A **4**, 5002 (2016).

[26] S. J. Zhang, S. S. Lin, X. Q. Li, X. Y. Liu, H. A. Wu, W. L. Xu, P. Wang, Z. Q. Wu, H. K. Zhong, and Z. J. Xu, Nanoscale **8**, 226 (2016).

[27] L. H. Li and Y. Chen, Adv. Funct. Mater. (2016).

[28] R. M. Granger II, H. M. Yochum, J. N. Granger, and K. D. Sienerth, *Instrumental Analysis* (Oxford University Press, New York, Oxford, 2017).

[29] F. Liang, H. Xu, X. Wu, C. Wang, C. Luo, and J. Zhang, Chinese Phys. B (2018).

[30] DoITPoMS, Univ. Cambridge (2007).

[31] V. Swaminathan and A. Jayaraman, in edited by K. H. J. Buschow, R. W. Cahn, M. C. Flemings, B. Ilschner, E. J. Kramer, S. Mahajan, and P. B. T.-E. of M. S. and T. Veyssière (Elsevier, Oxford, 2001), pp. 8387–8391.

[32] Univ. Sydney, (n.d.).

[33] Dept. Chem. Univ. California, Los Angeles (n.d.).

[34] M. Peeran and K. G. Srinivasamurthy, Chemvista.Org (2005).

[35] B. Robert, Photosynth. Res. **101**, 147 (2009).

[36] L. M. Malard, M. A. Pimenta, G. Dresselhaus, and M. S. Dresselhaus, Phys. Rep. **473**, 51 (2009).

[37] I. Childres, L. A. Jauregui, W. Park, H. Caoa, and Y. P. Chena, in *New Dev. Phot. Mater. Res.* (2013).

[38] Q. Cai, D. Scullion, A. Falin, K. Watanabe, T. Taniguchi, Y. Chen, E. J. G. Santos, and L. H. Li, Nanoscale **9**, 3059 (2017).

[39] X. Zhang, X.-F. Qiao, W. Shi, J.-B. Wu, D.-S. Jiang, and P.-H. Tan, Chem. Soc. Rev. **44**, 2757 (2015).

[40] R. Saito, Y. Tatsumi, S. Huang, X. Ling, and M. S. Dresselhaus, J. Phys. Condens. Matter (2016).

[41] A. McCreary, A. Berkdemir, J. Wang, M. A. Nguyen, A. L. Elías, N. Perea-López, K. Fujisawa, B. Kabius, V. Carozo, D. A. Cullen, T. E. Mallouk, J. Zhu, and M. Terrones, J. Mater. Res. (2016).

[42] A. Berkdemir, H. R. Gutiérrez, A. R. Botello-Méndez, N. Perea-López, A. L. Elías, C. I. Chia, B. Wang, V. H. Crespi, F. López-Urías, J. C. Charlier, H. Terrones, and M. Terrones, Sci. Rep. (2013).

[43] S. Mignuzzi, A. J. Pollard, N. Bonini, B. Brennan, I. S. Gilmore, M. A. Pimenta, D. Richards, and D. Roy, Phys. Rev. B - Condens. Matter Mater. Phys. (2015).

[44] A. J. McQuillan, Notes Rec. R. Soc. (2009).

[45] S. Laing, L. E. Jamieson, K. Faulds, and D. Graham, Nat. Rev. Chem. (2017).

[46] L. Jensen, C. M. Aikens, and G. C. Schatz, Chem. Soc. Rev. (2008).

[47] H. Yamada, H. Nagata, K. Toba, and Y. Nakao, Surf. Sci. (1987).

[48] M. Osawa, N. Matsuda, K. Yoshii, and I. Uchida, J. Phys. Chem. **98**, 12702 (1994).

[49] A. G. Brolo, D. E. Irish, G. Szymanski, and J. Lipkowski, Langmuir **14**, 517 (1998).

[50] K. I. Yoshida, T. Itoh, V. Biju, M. Ishikawa, and Y. Ozaki, Phys. Rev. B - Condens. Matter Mater. Phys. (2009).

[51] S. Yang, X. Dai, B. B. Stogin, and T. S. Wong, Proc. Natl. Acad. Sci. U. S. A. (2016).

[52] X. Ling, L. Xie, Y. Fang, H. Xu, H. Zhang, J. Kong, M. S. Dresselhaus, J. Zhang, and Z. Liu, Nano Lett. (2010).

[53] X. Ling and J. Zhang, Small (2010).

[54] G. W. Flynn, J. Chem. Phys. (2011).

[55] S. Huang, X. Ling, L. Liang, Y. Song, W. Fang, J. Zhang, J. Kong, V. Meunier, and M. S. Dresselhaus, Nano Lett. (2015).

[56] E. B. Barros and M. S. Dresselhaus, Phys. Rev. B - Condens. Matter Mater. Phys. (2014).

[57] Y. Lee, H. Kim, J. Lee, S. H. Yu, E. Hwang, C. Lee, J. H. Ahn, and J. H. Cho, Chem. Mater. (2016).

[58] C. Muehlethaler, C. R. Considine, V. Menon, W. C. Lin, Y. H. Lee, and J. R. Lombardi, ACS Photonics (2016).

[59] Y. Liu, Z. Gao, M. Chen, Y. Tan, and F. Chen, Adv. Funct. Mater. (2018).

[60] S. Huh, J. Park, Y. S. Kim, K. S. Kim, B. H. Hong, and J.-M. Nam, ACS Nano **5**, 9799 (2011).

[61] L. Sun, H. Hu, D. Zhan, J. Yan, L. Liu, J. S. Teguh, E. K. L. Yeow, P. S. Lee, and Z. Shen, Small (2014).

[62] N. Y. Kim, Y. C. Leem, S. H. Hong, J. H. Park, and S. Y. Yim, ACS Appl. Mater. Interfaces (2019).

[63] V. Valeš, P. Kovaříček, M. Fridrichová, X. Ji, X. Ling, J. Kong, M. S. Dresselhaus, and M. Kalbáč, 2D Mater. (2017).

[64] H. Zhao, Y. Zhang, G. Li, F. Tian, H. Tang, and R. Chen, RSC Adv. (2016).

[65] C. Zhou, W. Yang, and H. Zhu, J. Chem. Phys. (2015).

[66] K. Keyshar, M. Berg, X. Zhang, R. Vajtai, G. Gupta, C. K. Chan, T. E. Beechem, P. M. Ajayan, A. D. Mohite, and T. Ohta, ACS Nano (2017).

[67] A. Al-Rumaithi, (2019).

[68] K. Lai, Y. Zhang, R. Du, F. Zhai, B. A. Rasco, and Y. Huang, Sens. Instrum. Food Qual. Saf. (2011).

[69] F. Zhong, Z. Wu, J. Guo, and D. Jia, Nanomaterials (2018).

[70] X. Liu, Y. Shao, Y. Tang, and K. F. Yao, Sci. Rep. (2014).

[71] . L. Z., . F. Y., and . Y. jiannian, Trends Appl. Sci. Res. (2007).

[72] E. Wruss, L. Hörmann, and O. T. Hofmann, J. Phys. Chem. C **123**, 7118 (2019).

[73] H. Xu, L. Xie, H. Zhang, and J. Zhang, in *ACS Nano* (2011).

ACADEMIC VITA

Vivek Anil
(vivek3anil@gmail.com)

OBJECTIVE: To pursue research related to nanomaterials, condensed matter, biosensing, and optics

EDUCATION: B.S. Engineering Science & B.S. Physics
Graduated May 2020

Schreyer Honors College August 2016- Present

The Pennsylvania State University, University Park, PA

Relevant Courses Taken: Introduction to Electrical & Computer Engineering (Pre-college, Carnegie Mellon University), Product Development (Study Abroad, National University of Singapore), Electronic Properties & Applications of Materials, Intermediate Electricity & Magnetism, Quantum Mechanics I, Machine Learning (online Coursera class, Stanford University), Low Dimensional Nanoelectronics (graduate course), Solid State Physics I , Synthesis and Processing of Electronic and Photonic Materials

EXPERIENCE:

UNDERGRADUATE RESEARCHER

The Terrones Research Group, Penn State, Nov. 2016-Present

- Schreyer Honors Thesis (in-progress): Study graphene-enhanced Raman spectroscopy (GERS) for molecular detection applications; synthesize nitrogen doped graphene by chemical vapor deposition (CVD) and characterize Raman enhancement on test chemical dyes; develop MATLAB program to identify dyes based on spectral features
- Carbon Nanotube Super High Growth Project: Assist in construction of tunable biodevice to isolate different viruses with multi-walled carbon nanotubes; synthesize "super high" nanotubes (202.4 microns—longer than achieved heretofore so that more volume of the sample containing viruses can flow through the device); develop Python code for virus identification by analyzing Raman spectra of virus-enriched nanotubes

Cornell Nanoscale Facility, Shvets Group, Cornell University, June-Aug. 2018

- Worked as National Science Foundation-funded REU (Research Experience for Undergraduates) intern with postdoctoral mentors to fabricate a plasmonic metasurface to spectroscopically interrogate cancer cells
- Fabricated metasurfaces in cleanroom using electron-beam lithography, characterized metasurfaces using scanning electron microscopy, and assisted mentors with infrared spectra measurements
- Presented talk, poster at both Cornell University's 2018 REU Nano-Convocation and 2018 National Nanotechnology Coordinated Infrastructure REU Convocation at North Carolina State University; authored, submitted project report

Prof. Zhiwen Liu's Ultrafast and Nonlinear Optics Lab, Penn State, June-Aug. 2017

- Studied second harmonic generation in WS_2 monolayers for optical coating and cellular imaging applications
- Aided in setup for optics experiments; modified MATLAB code to automate stage translations and correct for uneven movements to enhance images; developed a

SolidWorks-model and 3D-printed crystalline structures and monolayers of transition metal dichalcogenides
- Presented poster at 7th Annual Undergraduate Research Symposium sponsored by the Department of Chemistry

SUMMER INTERN

Qorvo, Richardson (Dallas), TX, May- Aug. 2019
- Worked as engineering intern with the R&D group to develop a piezoelectric Bulk Acoustic Wave (BAW) biosensor
- Developed MATLAB programs to analyze data and act as checkpoints in biosensor production; specifically:
  - Compare devices' probe data to the specifications for parameters, such as frequency and mass sensitivity, and alert engineering and production about unsatisfactory devices
  - Create a script that automatically produces a yield map for each wafer and stores the map in a Datacon file
- Characterized device fabrication with wafer inspections and atomic force microscopy

SolePower (www.solepowertech.com), Pittsburgh, PA, July- Aug. 2016
- Designed, created a prototype for a sandal that helps people charge their phones by walking; embedded company's technology in sandal, made light-pack for demonstration, and researched how product could be marketed to electrically-poor regions like sub-Saharan Africa

SKILLS: Chemical Vapor Deposition synthesis, Electron-beam lithography, Scanning Electron Microscopy, Raman spectroscopy, Python, Java, MATLAB, SolidWorks, HAM Radio License

PUBLICATIONS & PRESENTATIONS
1. Granzier-Nakajima, T.; Fujisawa, K.; Anil, V.; Terrones, M.; Yeh, Y.-T. Controlling Nitrogen Doping in Graphene with Atomic Precision: Synthesis and Characterization. Nanomaterials 2019, 9, 425.
2. Anil, V., Huang, S., Shcherbakov, M., & Shvets, G. (2018). 2. Topics in Nano-Biophotonics: Fabrication of Plasmonic Metasurfaces that Attract and Spectroscopically Interrogate Cancer Cells. 2017-18 Cornell NanoScale Facility Research Accomplishments, 2–3.
3. Presentation: Topics in Nano-Biophotonics: Fabrication of Plasmonic Metasurfaces that Attract and Spectroscopically Interrogate Cancer Cells.
   a. Talk and poster session at 2018 National Nanotechnology Coordinated Infrastructure REU Convocation at North Carolina State University (August 2018)
   b. Talk and poster session at Cornell University (August 2018)
   c. Poster session at 2018 CNF Annual Meeting (October 2018)
   d. Poster session at Penn State Engineering Science & Mechanics ESM Today (January 2019).
4. Presentation: Robustness of Second Harmonic Generation in Monolayer Tungsten Disulfide.
   a. Poster session at 7th Annual Undergraduate Research Poster Symposium Sponsored by the Penn State Department of Chemistry and Central PA Section of the American Chemical Society (September 2017)

LEADERSHIP & INVOLVEMENT:

Learning assistant: Fluids and Thermal Physics and Wave Motion and Quantum Physics (PSU), (2017)

Coding project for Prof. Yuri Suhov, pertaining to stochastic matrices and optimization (PSU), (2017)

Co-leader Tracking, Mt. Lebanon High School Weather Balloon Project, (2014- 2015)

HONORS:

Honoree, Student Marshal: Physics, Spring Commencement at Penn State (2020)

Awardee, Honorable Mention NSF GRFP Competition (2020)

Recipient, John & Elizabeth Holmes-Teas Scholarship in Physics (2019-20)

Recipient, Joseph Marin Memorial Scholarship (2018-20),

Recipient, Schreyer Academic Excellence Scholarship (2016-20)

Recipient, President's Freshman Award (2017), President's Sparks Award (2018) for 4.0 GPA at Penn State; Dean's List (2016-19)

Recipient, Evan Pugh Scholar Award for being in the upper 0.5 percent of class at Penn State (2019)

Awardee, Erickson Discovery Grant: proposed graphene-based neuron study (declined, prior commitment at Cornell), (2018)

Recipient, Brown University Book Award for excellence in Written, Spoken Expression (2015)

Recipient, American Legion School Award and Sons of American Revolution School Award for citizenship (2012)